A performance comparison of heterostructure surface plasmon resonance biosensor for the diagnosis of novel coronavirus SARS-CoV-2

Tarik Bin Abdul Akib[1,2] · **Shahriar Mostufa**[1] · **Md. Masud Rana**[1] · **Md. Biplob Hossain**[3,4] · **Md. Rabiul Islam**[3]

Abstract

This paper presents a performance comparison of heterostructure surface plasmon resonance (SPR) biosensors for the application of Novel Coronavirus SARS-CoV-2 diagnosis. The comparison is performed and compared with the existing literature based on the performance parameters in terms of several prisms such as BaF_2, BK_7, CaF_2, CsF, SF_6, and SiO_2, several adhesion layers such as TiO_2, Chromium, plasmonic metals such as Ag, Au, and two-dimensional (2D) transition metal dichalcogenides materials such as BP, Graphene, $PtSe_2$ MoS_2, $MoSe_2$, WS_2, WSe_2. To study the performance of the heterostructure SPR sensor, the transfer matrix method is applied, and to analyses, the electric field intensity near the graphene-sensing layer contact, the finite-difference time-domain approach is utilized. Numerical results show that the heterostructure comprised of CaF_2/TiO_2/Ag/BP/Graphene/Sensing-layer has the best sensitivity and detection accuracy. The proposed sensor has an angle shift sensitivity of 390°/refractive index unit (RIU). Furthermore, the sensor achieved a detection accuracy of 0.464, a quality factor of 92.86/RIU, a figure of merit of 87.95, and a combined sensitive factor of 85.28. Furthermore, varied concentrations (0–1000 nM) of biomolecule binding interactions between ligands and analytes have been observed for the prospects of diagnosis of the SARS-CoV-2 virus. Results demonstrate that the proposed sensor is well suited for real-time and label-free detection particularly SARS-CoV-2 virus detection.

Keywords Biosensor · Finite-difference time-domain (FDTD) · SARS-CoV-2 virus · Surface plasmon resonance · 2D materials · Transfer matrix method

1 Introduction

The severe acute respiratory syndrome coronavirus 2 (SARSCoV2) is a dangerous and infectious single-stranded ribonucleic acid (RNA) virus that causes respiratory illness in humans. SARS-CoV-2 is a coronavirus strain that the World Health Organization (WHO)

✉ Md. Biplob Hossain
  biplobh.eee10@gmail.com

Extended author information available on the last page of the article

has declared a worldwide pandemic due to its role in the ongoing COVID-19 (Coronavirus disease 2019) pandemic (Qureshi et al. 2021; Douedi and Miskoff 2020). So far, over 626 million people have tested positive for COVID-19, and over 6.56 million have died as a result of the virus (World Health Organization 2022). Notably, malignant variants of SARS-CoV-2 have emerged, including alpha (B.1.1.7), beta (B.1.351), gamma (P.1), delta (B.1.617.2), delta plus (B.1.617.2.1/ (AY.1), and omicron (B.1.1.529). All variants have four important proteins: spike glycoprotein (S), nucleocapsid protein (N), an envelope protein (E), and membrane protein (M). spike glycoproteins are divided into two subunits known as S1 and S2 proteins. The S1 protein is primarily responsible for interacting with the human angiotensin-converting enzyme 2 (ACE2) host cell receptor, whereas the S2 protein is responsible for membrane fusion (Hassanpour and Nikbakht 2021; Astuti and Ysrafil 2020; Wong et al. 2004; Huang et al. 2020; Weir 2020). More intriguingly, in the new variants of SARS-CoV-2, the significant changes naturally acquired in the spike mutation more effectually attach to the human ACE2 receptor, and these new variants become a more contagious virus. The human ACE2 receptor access the SARS-CoV-2 virus S protein to enter the cell, the virus spreading by replicating the genome sequence and causing immense damage to the brain, heart, kidneys, liver, lung, and spleen. Accordingly, the neutralization of virus S protein is the main target in clinical research. Additionally, permitted vaccination, early diagnosis, and supervision are crucial for preventing the COVID-19 pandemic. In Bangladesh, over 318 million vaccine doses have been delivered (World Health Organization 2022), and current statistics show that immunizations provide effective protection against the COVID-19 virus and mortality. The changes in the SARS-CoV-2 strains resulted in lower strain coverage tests and false-negative PCR test findings. Many ways for identifying SARS-CoV-2 viruses are known in the literature, however significant complexities limit their practical use. These complexities have low detection accuracy and sensitivity, are dependent on sample preparation and sanitization, are time-consuming, require advanced instruments and accessories, have a high maintenance cost, are available on a large scale, require technically qualified personnel, and are not suitable for rapid, real-time analysis.

Recently SPR is one of the most promising and susceptible optical-based sensing devices which is used to identify SARS-CoV-2 viruses due to its very high sensitivity and more user-friendly mechanism (Talebian et al. 2020; Akib et al. 2021; Pandey et al. 2022; Nor et al. 2021; Lim et al. 2021; Mostufa et al. 2022a; Maddali et al. 2021; Chen et al. 2021). Furthermore, this sensor has practically been implemented for multiple applications (Alharbi et al. 2019; Nangare and Patil 2021; Mostufa et al. 2021, 2022, 2022b), for example (Chaudhary et al. 2021; Thakallapelli et al. 2016; Campbell and Kim 2007; Englebienne et al. 2003; Kitenge et al. 2009; Zhang et al. 2007; Nielsen et al. 2000). However, researchers are still working on the development of new structures and designs to form a sophisticated SPR sensor in different sensing applications (Zhang et al. 2022; Eslami-Kaliji et al. 2022). SPR-based sensors are used in most biomedical detection due to their susceptibility to the sensing medium's refractive index (RI) change that is in direct contact with SPR-based sensor metal films (Dai et al. 2019; Bochenkov et al. 2013). The SPR sensor works on the basis of the oscillations of the free electrons, which is also known as surface plasmon (SP). In surface plasmon (SP) mode, the interaction between the dielectric medium and metal occurs because of having an opposite real value of dielectric constants resulting in free-electron oscillations (Dai et al. 2019). When a TM or p-polarized light incident on the prism and reflects from the metal film, it excites the surface plasmons and generates oscillations of electrons. The SP wave (SPW) responds to changes in the analyte's refractive index. The SPR curve, which relates reflectance to incidence

angle, is particularly sensitive to changes in the sensor interface's refractive index. The SPR signal will fluctuate dramatically in response to even a little change in the sensing medium's refractive index. High sensitivity is needed for an SPR biosensor to perform well. For resonance or SPR angle conditions, the output reflectance intensity is reduced to a minimum level due to the maximum electron excitation of surface plasmons (SP). Due to strong localization and exponentially decaying evanescent waves over the metal film interface (Dey et al. 2021; Nisha et al. 2019). The traditional Kretschmann arrangement of simple metal does not have the same sensing capabilities as today's hybrid construction. This is due to the fact that a metal layer alone cannot absorb larger excitations of light energy. However, transition metal dichalcogenides (TMDC) materials may absorb more light energy because their dielectric constant has a large real part and a small imaginary part value, resulting in intense light-matter interaction. Furthermore, a metal layer coated with TMDC materials improved the sensor's detecting stability (Maurya et al. 2018). Two-dimensional (2D) materials such as graphene, black phosphorus (BP), and TMDCs (MoS_2, WS_2, $MoSe_2$, WSe_2) have received a lot of attention in recent years due to their unique electrical and optical properties. The use of graphene and TMDCs in sensing technologies has sparked widespread attention. Many studies have already proposed hybridization of the prism-coupled structure using the Kretschmann configuration to improve sensor detection accuracy, sensitivity, and speed (Katyal and Soni 2014). Moreover, the improvement of device performance utilizing a hybrid structure had also been reported by many researchers (Rahman et al. 2017; Hasib et al. 2019; Maurya et al. 2015a). For instance, the extremely sensitive graphene-based SPR sensor suggested by Wu et al. (2010) is capable of enhancing the overall sensitivity to 25%. Again, based on graphene-MoS_2 Zeng et al. (2015) suggested SPR nanostructured biosensors with enhanced sensitivity, and Ouyang et al. (2016) illustrated TMDC / Silicon nano-sized SPR sensors. Finally, the author, Rahman et al. (2020) had shown sensitivity increment using the heterostructure of WS_2 layer with gold (Au) as plasmonic material to improve sensitivity significantly. Therefore, all these previously reported works suggested that the TMDCs with graphene are outstanding candidates for sensitivity enhancement of the Kretschmann configuration SPR-based sensors. The performance of these nanostructure devices has greatly increased as a result of recent advancements in nanostructure production technology. As a result, the Kretschmann configuration structure-based angle interrogation approach has emerged as the most promising method for a variety of sensing applications (Ahmadivand et al. 2016; Chamoli et al. 2020). From the comparison with some recently reported hybrid SPR-based sensor sensing parameters, our proposed model exhibits the highest sensitivity. For instance, Wang et al. (2017) proposed a prism/Ag/Au/ WS_2/graphene material layered sensor with angular sensitivity of 182.5 deg/RIU where our proposed model exhibits 202.82 deg/RIU. Similarly, Lin proposed a hybrid Prism/Au/MoS_2/WS_2/WSe_2 material layer sensor with angular shift sensitivity of 142 deg/RIU (Lin et al. 2020). Again, M. Mahbub et al. proposed a WS_2 layer interrogation sensor prism/Ag/ $PtSe_2$/WS_2 material layered and showed maximum sensitivity of 194 deg/RIU (Rahman et al. 2020). Finally, to measure urine glucose with angular shift sensitivity of 194.12 deg/RIU (Mudgal et al. 2020) using prism/ MoS_2/h-BN/ graphene material layered structure, N. Mudgal et al. reported a hybrid structure having four-layer that consists of molybdenum disulfide (MoS_2), h-BN (hexagonal boron nitride), Au, and graphene.

Furthermore, because of its wide range of adjustable direct bandgap, high carrier mobility, and remarkable electrical, optical, and phonon characteristics, black phosphorus (BP), a potential new 2D material, has received a lot of interest since it was introduced to the 2D material family in 2014 (Dai et al. 2019). When a few-layer BP is deposited on the surface of a metal

film, the significant real component of its refractive index results in a notable improvement in sensitivity. We covered the metal film used in this research with heterostructures of few-layer BP/graphene to boost its sensitivity. Furthermore, the graphene layer on the sensor surface has good conductivity as well as the capacity to stably adsorb biomolecules. The abundant carbon-based rings in biomolecules are the primary cause of a biomolecule's absorption by a graphene layer. The p-stacking interactions between graphene hexagonal cells and carbon-based ring structures are frequently prevalent in bio/nano-molecules in addition to possessing a unique chemical structure (Song et al. 2010; Artiles et al. 2011).

To find the best-optimized sensitivity and detection accuracy of the proposed sensor has been analyzed with different prisms (BaF_2, BK_7, CaF_2, CsF, SF_6, and SiO_2) for light coupling, an adhesion layer (TiO_2, Chromium), plasmonic metals (Ag, Au), two-dimensional (2D) and transition metal dichalcogenides (TMDCs) materials (BP, Graphene, $PtSe_2$ MoS_2, $MoSe_2$, WS_2, WSe_2) materials. From the comparative analysis, it has been found that $CaF_2/TiO_2/Ag/BP/Graphene/Sensing-layer$ structure of the proposed sensor achieved the maximum angular shift sensitivity up to 390°/refractive index unit (RIU). In addition, the sensor acquired a detection accuracy (DA) of 0.464, a quality factor (QF) of 92.86/RIU, a figure of merit (FOM) of 87.95, and an overall SPR's combined sensitive factor (CSF) of 85.28. Additionally, it has also been demonstrated that the proposed sensor can diagnose the SARS-CoV-2 virus by detecting the binding interactions between specified ligands and various concentrations of target analytes.

The main contributions of this article are:

- The highly sensitive heterostructure ($CaF_2/TiO_2/Ag/BP/Graphene/Sensing-layer$) SPR sensor is proposed for the detection of target biomolecules.
- The high plasmonic properties-based 2D TMDC materials have been utilized in the proposed SPR sensor.
- The heterostructure SPR sensor has been comprehensively investigated with different prisms, plasmonic metals, an adhesion layer, and 2D TMDC materials layers to increase the performance, sensitivity, and detection accuracy.
- The strategy has been well-defined for the detection of the SARS-CoV-2 virus.
- Finally, the output results are assessed during the adsorption of target analytes. The results show the proposed sensor is well suited for real-time and label-free detection particularly SARS-CoV-2 virus detection.

The paper is organized as follows: Sect. 2 emphasizes the proposed sensor modeling, TMM algorithm, and performance measuring parameter used to analyze the proposed sensor. Section 3 introduces the FDTD technique to analyze the performance of the proposed sensor. Section 4 shows results under a variety of scenarios. Section 5 describes the target analytes for the detection of the SARS-CoV-2 virus, Sect. 6., describes the real-time detection techniques of target analytes, respectively, and Sect. 7 brings this work to a conclusion.

2 Sensor design and numerical modeling

2.1 Design of the proposed sensor

The purpose of using CaF_2 layer is a high competitor for prism substrate in SPR sensors and contains many features such as high transmission (above 90%) of the incident light at

the metal surface, less Fresnel loss, small dispersion, and less temperature dependence of RI (Malitson 1963; Saad 2009; Yadav and Jain 2016). The second layer, titanium dioxide (TiO_2) is used as an adhesion thin film to provide strong interaction between the prism and plasmonic metal layer, enhance the RI sensitivity, and tune the resonance wavelength (Panda and Pukhrambam 2021; Singh and Prajapati 2020; Wang et al. 2019). Principally, a silver (Ag) layer is used as a plasmonic metal substrate. Notably, black phosphorus (BP) is a new auspicious 2D material and holds excellent optoelectrical and phonon properties, such as widely tunable and direct bandgap, higher carrier mobility, electronic bridging, and stronger binding of receptors and analytes (Nangare and Patil 2023; Wu et al. 2017). Fascinatingly, BP-coated nanostructure molecular sensing responses are 40 times faster than other 2D materials (Nangare and Patil 2023). The graphene film is coated on the surface of the BP thin film as a biomolecule recognition element (BRE). Remarkably, the graphene layer has high conductivity, high carrier mobility, van der Waals force bond, and improved biomolecule absorption on the sensing surface due to its π–π stacking with the carbon ring-based lattice structure of the analytes (Nangare and Patil 2023; Zhu et al. 2021). The proposed structure of the SPR sensor has been shown in the schematic diagram of Fig. 1. As well, the polarizers play an important role in SPR systems. They help align the incident light into a linear polarization before it reaches the SPR structure, allowing for more precise and accurate measurements. SPR only occurs in linearly polarized light, and the use of a polarizer helps eliminate any confusion caused by randomly polarized light, enhancing the sensitivity and reliability of SPR readings. At a particular incident wavelength (λ) of 632.8 nm on the prism, the RI of the CaF_2 prism and TiO_2 adhesion layer can be calculated through the ensuing (1) and (2) as follows (Panda and Pukhrambam 2021; Kushwaha et al. 2018):

$$n_{CaF_2} = \sqrt{1 + \frac{0.567888\lambda^2}{\lambda^2 - 0.0502636^2} + \frac{0.471091\lambda^2}{\lambda^2 - 0.100390^2} + \frac{3.848472\lambda^2}{\lambda^2 - 34.649040^2}} \tag{1}$$

$$n_{TiO_2} = \sqrt{5.913 + \frac{0.2441}{\lambda^2 - 0.0803}} \tag{2}$$

Similarly, At a wavelength (λ), the RI of plasmonic metal (Ag or Au) can be computed from the Drude–Lorentz model (Rahman et al. 2020, 2021; Panda and Pukhrambam 2021; Wu et al. 2017; Jia et al. 2019, 2022):

Fig. 1 Schematic diagram of the proposed six-layered (CaF_2/TiO_2/Ag/BP/Graphene/Sensing-layer) SPR sensor for diagnosis of biomolecules
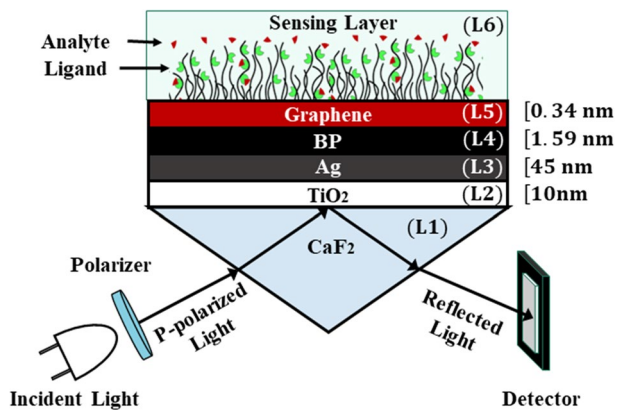
$$n_{\text{metal}} = \sqrt{1 - \frac{\Lambda_c \lambda^2}{\Lambda_p^2 (\Lambda_c + i\lambda)}} \tag{3}$$

$$n_{\text{Ag}} = \sqrt{1 - \frac{(1.7614 \times 10^{-5})\lambda^2}{(1.4541 \times 10^{-7})^2 (1.7614 \times 10^{-5} + i\lambda)}} \tag{4}$$

In (3), Λ_c and Λ_p denote the collision and plasma wavelengths, respectively. The values of Λ_c and Λ_p for Ag are 1.7614×10^{-5} m and 1.4541×10^{-7} m.

The TMDC materials form a van der Waals force with a graphene layer, which is used to enhance absorption and sensitivity. The RI of other layers consisting of TMDC materials is collected from the reference (Panda and Pukhrambam 2021; Park et al. 2012). Moreover, the refractive index of TMDCs (Ouyang et al. 2016; Wu et al. 2017) at $\lambda = 632.8$ nm is shown in Table 1. Furthermore, the multi-Lorentzian function is employed to acquire the dielectric function of MX_2, which can be specified as (Panda and Pukhrambam 2021; Gan et al. 2019). The wavelength dependent on the dielectric function of $MoSe_2$, WSe_2, MoS_2, and WS_2 monolayer can be fitted by the multi-Lorentzian model:

$$\varepsilon(E) = 1 + \sum_{m=1}^{N} \frac{f_m}{E_m^2 - E^2 - iE_{\gamma_m}} \tag{5}$$

In (5), $E(eV) = 1.2398/\lambda(\mu m)$ represents the photon energy, the model parameters f_m, E_m and γ_m signify the oscillation strength, resonance energy, and spectral width of mth oscillation respectively and their values can be computed from the experimental data presented (Kravets et al. 2017). Additionally, graphene's hexagonal-shaped ordered carbon atoms structure ensures good contact with the analyte or biological sample molecules, increasing the sensitivity of the suggested sensor as a 2D material. The contact between the probe ligands and the graphene layer is increased. The ligand can be immobilized on a graphene surface using PBASE. The following expression can be used to calculate the RI of the graphene layer at 632.8 nm:

$$n_G = 3.0 + \frac{iC_1 \lambda}{3}, (C_1 \approx 5.446\,\mu m^{-1}) \tag{6}$$

The refractive index of the sensing medium is taken as n_s of $1.3348 + \Delta n$ (Here, $\Delta n = 0.005$), where Δn is the change of the refractive index in the sensing medium due to the occurrence of a biological or biochemical interaction. The authors in reference (Akib et al. 2021; Chabot et al. 2012; Isaacs and Abdulhalim 2015) present information on the formation of various thin film layers utilizing contemporary methods including sol–gel, sputtering, physical vapor deposition (PVD), and chemical vapor deposition (CVD). The paper also offers comprehensive details on the procedures and evaluation of the different thin films as well as a concise explanation of the possible method for attaching the specific probe ligand to the sensor surface for interaction with target biomolecules.

Table 1 The refractive indexes and thickness of the material at a wavelength of 632.8 nm

Layer Order	Materials	No. of layers [L]	Thickness of layer [nm]	Refractive index	References
1st Layer (Prism)	BaF$_2$	1	7950	1.4733	Li (1976)
	BK$_7$	1		1.5151	Kumar et al. (2022)
	CaF$_2$	1		1.4329	Panda and Pukhrambam (2021)
	CsF	1		1.4768	Li (1976)
	SF$_6$	1		1.799	Park et al. (2012)
	SiO$_2$	1		1.4607	Li (1976)
2nd Layer (Adhesion)	TiO$_2$	1	10	1.99	Panda and Pukhrambam (2021)
	Chromium	1	2	3.135+3.310i	Park et al. (2012)
3rd Layer (Metal)	Ag	1	45	0.0803+4.2347i	Kumar et al. (2022)
	Au	1	45	0.1378+3.6196i	Kumar et al. (2022)
4th & 5th Layer (2D TMDC materials)	PtSe$_2$	6	L×0.375(monolayer) ≈ 2	2.9029+0.8905i	Guo et al. (2020)
		11	L×0.375(monolayer) ≈ 4	2.9161+1.2986i	Panda and Pukhrambam (2021), Guo et al. (2020)
		16	L×0.375(monolayer) = 6	3.0168+1.6734i	Guo et al. (2020)
	BP	1, 3, 5	L×0.53(monolayer) = 0.53, 1.59, 2.65	3.5+0.01i	Park et al. (2012)
	MoS$_2$	1, 3, 5	L×0.65(monolayer) = 0.65, 1.95, 3.25	5.0805+1.1723i	Panda and Pukhrambam (2021), Park et al. (2012), Nurrohman and Chiu (2020)
	MoSe$_2$	1, 3, 5	L×0.70(monolayer) = 0.70, 2.1, 3.5	4.62+1.0063i	Park et al. (2012)
	WS$_2$	1, 3, 5	L×0.80(monolayer) = 0.80, 2.4, 4	4.9+0.3124i	Panda and Pukhrambam (2021), Park et al. (2012)
	WSe$_2$	1, 3, 5	L×0.70(monolayer) = 0.70, 2.1, 3.5	4.5501+0.4332i	Park et al. (2012), Nurrohman and Chiu (2020)
	Graphene	1, 3, 5	L×0.34(monolayer) = 0.34, 1.02, 1.7	3.0+1.1491i	Panda and Pukhrambam (2021), Park et al. (2012), Nurrohman and Chiu (2020)
6th Layer (Sensing)	MXene	4, 7, 9, 12	L×0.993(monolayer)	2.38+1.33i	Kumar et al. (2021, 2022)
	Analyte	-	2	1.3348 + Δn	-
				$\Delta n = \|1.3348 - 1.3398\| = 0.005$	

2.2 Numerical modeling for simulation

2.2.1 Reflectivity (R$_p$) calculation

In this work, the proposed sensor structure (CaF$_2$/TiO$_2$/Ag/BP/Graphene/Sensing–layer) is based on the renowned Kretschmann's attenuated total reflection (ATR) structure. The light incident at the prism-metal interface and totally reflected from the base of the BK$_7$ prism. The reflective intensity of the proposed Fresnel N-layer model is calculated by using the transfer matrix method (TMM). However, for analyzing the proposed sensor, the boundary conditions of the tangential component are considered with the initial limit of $Z = Z_1 = 0$, and the final limit of Z_{N-1}, thereby giving rise to (7) can be followed as:

$$\begin{bmatrix} E \\ H \end{bmatrix} = F_{ij} \begin{bmatrix} E_{N-1} \\ H_{N-1} \end{bmatrix} \tag{7}$$

In (7), E_1, E_{N-1} and H_1, H_{N-1} indicate the tangential electric and magnetic field components of the first and the Nth layers, respectively. F_{ij} denotes the transfer matrix attribute of the Fresnel N-layer model. For the TM light, the transfer matrix attribute can be described by:

$$F_{ij} = \left[\prod_{K=2}^{N-1} F_k \right]_{ij} = \begin{bmatrix} F_{11} & F_{12} \\ F_{21} & F_{22} \end{bmatrix} \tag{8}$$

$$\text{With,} \quad F_k = \begin{bmatrix} \cos\beta_k & (-i\sin\beta_k)/q_k \\ -iq_k\sin\beta_k & \cos\beta_k \end{bmatrix} \tag{9}$$

$$\beta_k = \frac{2\pi d_k}{\lambda} \sqrt{(\varepsilon_k - n_1^2\sin^2\theta_1)} \tag{10}$$

$$q_k = \sqrt{\frac{\mu_k}{\varepsilon_k}} \tag{11}$$

$$\cos\theta_k = \frac{\sqrt{(\varepsilon_k - n_1^2\sin^2\theta_1)}}{\varepsilon_k} \tag{12}$$

In (9–12), $\varepsilon_k, \beta_k, \theta_k, d_k$ are the dielectric constant, phase constant, angle of an entrance, and depth of the kth layer, respectively. In accordance with Fresnel's equations, the complex reflection coefficient (r_p) of p-polarized TM incident electromagnetic field can be expressed by,

$$r_p = \frac{(F_{11} + F_{12}q_N)q_1 - (F_{21} + F_{22}q_N)}{(F_{11} + F_{12}q_N)q_1 + (F_{21} + F_{22}q_N)} \tag{13}$$

In (13), q_1 and q_N represents the relative components of the first layer and the Nth layer respectively. Therefore, the system reflectivity Rp for the p-polarized incident light can then

be obtained by taking the square of the reflection coefficient r_p. The reflection intensity of p-polarized incident light can be denoted as (Nurrohman and Chiu 2020):

$$R_p = \left| r_p^2 \right| \tag{14}$$

The propagation constant (β_{spw}) of SPW is changed with the immobilization of analytes in the sensing region. This propagation constant can be described as:

$$\beta_{spw} = \frac{2\pi}{\lambda_{light}} \sqrt{\frac{n_m^2 n_a^2}{n_m^2 + n_a^2}} \tag{15}$$

In (15), n_m and n_a represent the RI of the plasmonic material and the sensing medium, respectively. The ratio of reflectance and incidence angle is familiar to the SPR curve. The incident angle is recognized as the θ_{SPR}, which can be expressed as:

$$\theta_{SPR} = \sin^{-1}\left(\frac{1}{n_{Prism}} \sqrt{\frac{n_m^2 n_a^2}{n_m^2 + n_a^2}} \right) \tag{16}$$

$$\theta_{SPR} = \sin^{-1}\left(\frac{1}{n_{CaF_2}} \sqrt[5]{\frac{n_{TiO_2}^2 n_{Ag}^2 n_{BP}^2 n_G^2 n_s^2}{n_{TiO_2}^2 + n_{Ag}^2 + n_{BP}^2 + n_G^2 + n_s^2}} \right) \tag{17}$$

In (17), $n_{TiO_2}, n_{Ag}, n_{BP}, n_G$, and n_S are the RI of the TiO$_2$, Ag, BP, and graphene thin film, respectively. Here, De Moivre's formula (Cho 1998; Lial et al. 2012) is used to calculate the nth roots of complex numbers. It is also employed in the examination of the reflection of light at surfaces. By utilizing De Moivre's formula, the reflection coefficient can be expressed as a complex number, making the analysis and visualization of the material's reflection behavior easier.

2.2.2 Performance measuring parameters

The proficiency of the SPR sensors is categorized on the basis of sensitivity (*S*), full width at half maximum (FWHM), DA, FOM, QF and CSF parameters. Sensitivity, quality factor, and detection accuracy are considered the most important sensing parameters to judge the performance of a sensor. The angular sensitivity (*S*) is described as the ratio of change in the SPR angle ($\Delta\theta_{res}$) to the variation in analyte RI (Δn), which can be expressed as below (18).

$$S = \frac{\Delta\theta_{SPR}}{\Delta n_s} \text{ [deg/RIU]} \tag{18}$$

The FWHM indicates the linewidth of the SPR reflectance curve. The narrower FWHM indicates detecting the specific resonance angle shift more accurately. Therefore, it is crucial to maintain FWHM as minimum as possible because depending on FWHM other parameters DA, Quality factor, FOM, and CSF also vary.

$$FWHM = \Delta\theta_{0.5} \text{ [deg]} \tag{19}$$

Again, the quality factor (QF) is measured by dividing angular sensitivity by the full width half maximum (FWHM) of the SPR curve, which is expressed as, QF (RIU^{-1}) (20).

$$QF = \frac{S}{FWHM}\left[RIU^{-1}\right]$$

(20)

The detection accuracy (DA) is computed as the ratio of $\Delta\theta_{SPR}$ and FWHM (Panda and Pukhrambam 2021; Rahman et al. 2021, 2017; Yesudasu and Pradhan 2021; Akib et al. 2021).

$$DA = \frac{\Delta\theta_{SPR}}{FWHM}$$

(21)

The Figure of Merit (FOM) is another scale used to determine the sensing efficiency. The ultimate goal is to find the optimal combination of materials, design, and conditions that result in a high FOM, signifying high efficiency, sensitivity, and overall performance, The expression of FOM can be found in Eq. (22).

$$FOM = \frac{S \times \left(1 - R_{min}\right)}{FWHM}$$

(22)

Eventually, the CSF provides a comprehensive evaluation of the sensor's quality and performance, taking into account various aspects such as sensitivity, stability, and selectivity. In other words, the overall performance of the sensor is represented by the CSF, as stated in Eq. (23) (Yesudasu and Pradhan 2021).

$$CSF = \frac{S \times \left(R_{max} - R_{min}\right)}{FWHM}$$

(23)

3 FDTD method for the proposed sensor

The finite-difference time domain (FDTD) is a numerical technique to analyze the electromagnetic field of the proposed sensor by using commercial Lumerical FDTD solutions. In the FDTD technique, the YEE algorithm is applied to solve Maxwell's equation. Figure 2 shows the proposed SPR sensor ($CaF_2/TiO_2/Ag/BP/Graphene/$-Sensing–layer) structure design in Lumerical FDTD solution. The objects editor of the FDTD technique sets the mesh as a non-uniform mesh and all other utilized parameters as default to enhance accuracy. The perfectly matched layer (PML) absorbing boundary conditions are set to absorb incident light with minimum reflections, and the DFT monitor is set to evaluate the reflection and transmission. Notably, the simulation time is set to 1000 (fs) at temperature 300 K, background RI is set to 1.00, and the angle of incidence sweep from 30° to 70° angle. Moreover, the design parameters for the proposed sensor are manifested in Table 2.

In reference (Akib et al. 2021), the correlation between the TMM and FDTD analysis was revealed for SPR sensor analysis. The FDTD simulation provides a visual representation of electric and magnetic field propagation, making it a better option for observing the impact of a multi-layered SPR structure. The proposed sensor underwent a numerical investigation using both TMM and FDTD methods, with the TMM encrypted in MATLAB using the TMM algorithm. The performance of the proposed sensor was validated using TMM and confirmed with FDTD, both resulting in similar results for detecting the SARS-CoV-2 virus.
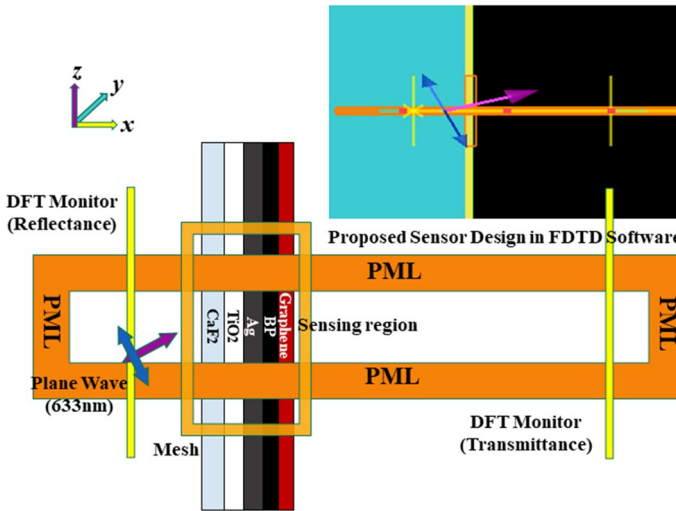
Fig. 2 The proposed SPR sensor in FDTD solution

4 Results and discussion

4.1 Effect of different prisms on sensing performance (Prism/Ag/Analyte—1.3348)

The purpose of using CaF_2 layer is a high competitor for prism substrate in SPR sensors and contains many features such as high transmission (above 90%) of the incident light at the metal surface, less Fresnel loss, small dispersion, and less temperature dependence of RI (Malitson 1963; Saad 2009; Yadav and Jain 2016). The effect of BaF_2, BK_7, CaF_2, CsF, SF_6, and SiO_2 prism material for the Prism/Ag/Analyte (1.3348) structure has been shown in Fig. 3 and the data are tabulated in Table 3.

The SPR curves exhibit the resonance angle change for BaF_2, BK_7, CaF_2, CsF, SF_6, and SiO_2 prism and for CaF_2 the highest sensor parameters are observed. From the numerical results comparing various prisms, it has been obtained that the CaF_2 prism exhibits the highest sensors sensitivity and minimum reflectance, as shown in Fig. 3a, as well as it can be inferred that the prism is CaF_2 the best-suited coupling substrate amongst the other discussed prisms for achieving significantly enhanced angular sensitivity, FOM, DA, QF, and CSF, as shown in Fig. 3b–d.

4.2 Effect of second layer on sensing performance (CaF₂/2nd Layer/Ag/Analyte—1.3348)

To find the best adhesion layer sensing performance the numerical analysis has been carried out by adding TiO_2 and Chromium (Cr). The obtained result for CaF_2/2nd Layer/Ag/Analyte structure has been shown in Fig. 4 and the results data tabulated in Table 4. In Fig. 4a, it is clearly seen that adding TiO_2 as a second layer shows the highest sensitivity and minimum reflectance intensity. Moreover, the DA and FOM exhibited by TiO_2 compared to chromium are much higher as well as the highest QF and CSF are achieved, as

Table 2 Design parameters of the proposed sensor structure using FDTD

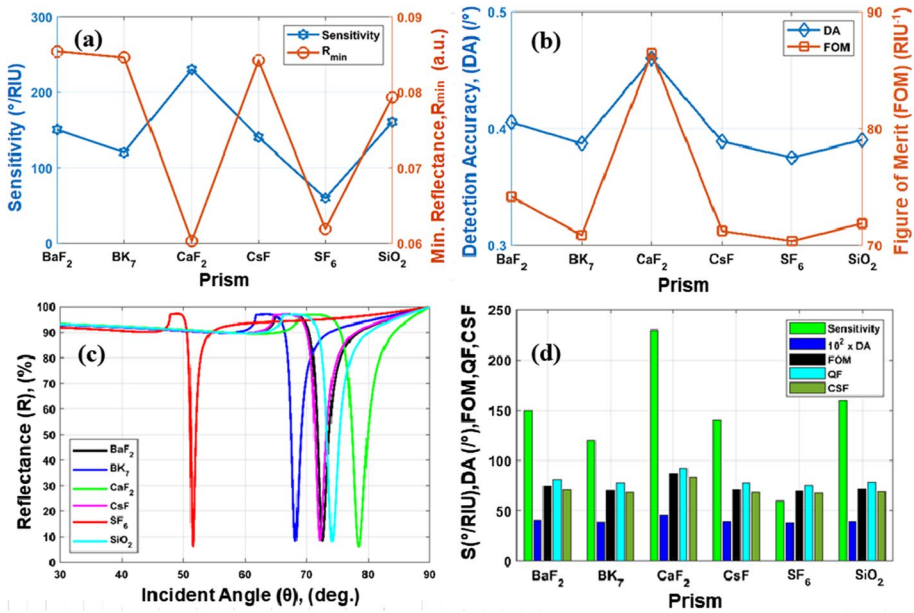| Layer	X_{min}	X_{max}	X_{span}	Y_{min}	Y_{max}	Y_{span}	Z_{min}	Z_{max}	Z_{span}	Additional Parameters
CaF$_2$	− 8	− 0.05	7.95	−1	1	2	− 0.5	0.5	1	Simulation time: 1000 fs; Simulation temperature: 300 k; Stability Factor: 0.99; Time Step: 0.00735722; Boundary Condition:—X: PML and Y: Bloch;
TiO$_2$	− 0.05	− 0.04	0.01	− 1	1	2	− 0.5	0.5	1	
Ag	− 0.04	0.005	0.045	− 1	1	2	− 0.5	0.5	1	
BP	0.005	0.00659	0.00159	− 1	1	2	− 0.5	0.5	1	
Graphene	0.00659	0.00693	0.00034	− 1	1	2	− 0.5	0.5	1	
Analyte	0.00693	0.00893	0.002	− 1	1	2	− 0.5	0.5	1	
FDTD	− 0.5	1	1.5	− 0.00125	0.00125	0.0025	–	–	–	Maximum override x mesh: dx (0.005 µm)
Mesh	− 0.05	0.00893	0.05893	− 0.25	0.25	0.5	− 5E−08	5E−08	1E−07	
Source	− 0.2			− 0.0025	0.0025	0.005	− 1	1	2	Source: Plane wave; X- axis in a forward direction; Wavelength 0.633 µm
Time monitor	− 0.425	–		–	–		–	–	–	Data record: E_x, E_y, E_z, H_x, H_y, H_z, Power
Reflectance	− 0.425	0		0			0			
Transmittance	1	0		0			0			

Fig. 3 **a** Angular Sensitivity and minimum reflectance (R_{min}), **b** DA and FOM, **c** SPR characteristic curve, and **d** Overall performance of SPR sensor for BaF_2, BK_7, CaF_2, CsF, SF_6, and SiO_2 prism, considering at sensing layer refractive index, n_s of 1.3348

shown in Fig. 4b–d. So, from the results, the TiO_2 is perfect as the second layer as it exhibits the highest sensor performance.

4.3 Effect of different metal layers on sensing performance (CaF_2/ TiO_2/Metal (Au, Ag)/Analyte—1.3348)

The charge carrier densities of metals play a very important role in SPs generation. Not only that, but metal's behavior in the outside environment also affects sensor performance. The effects of different plasmonic metals (Au, Ag) on the proposed SPR sensor are shown in Fig. 5a–d, and obtained results are tabulated in Table 5. The numerical result shows that Au exhibits high angular shift sensitivity compared to Ag however other crucial sensor parameters such as FOM, DA, QF, and CSF reduce drastically using Au. Therefore, considering overall sensor performance, Ag is taken as a plasmonic layer and after adding 2D and TMDC material in the next section the proposed sensor has managed to achieve desired angular sensitivity with the highest DA, FOM, QF, and CSF.

Remarkably, In Fig. 5a, the Au layer has the highest sensitivity, but in terms of detection accuracy, FOM, QF, and CSF, the Ag layer has best optimized performance, as shown in Fig. 5b–d. So, from the results, the Ag is taken as the plasmonic metal layer in the proposed SPR sensor.

Table 3 Comparison of various prism materials for various sensor parameters

Prism	Metal/Analyte	θ_1	θ_2	$\Delta\theta_{SPR}$	R_{min}	R_{max}	Sensitivity (S)	FWHM	DA	FOM	QF	CSF
BaF$_2$	Ag/Analyte,$\Delta n = |1.3348 - 1.3398| = 0.005$	72.6	73.35	0.75	0.0854	0.9689	150	1.85	0.4054	74.1568	81.0811	71.6351
BK$_7$		68.2	68.8	0.6	0.0846	0.9695	120	1.55	0.3870	70.8697	77.4193	68.5084
CaF$_2$		**78.5**	**79.65**	**1.15**	**0.0603**	**0.9683**	**230**	**2.5**	**0.46**	**86.4524**	**92**	**83.536**
CsF		72.2	72.9	0.7	0.0842	0.9688	140	1.8	0.3889	71.2289	77.7778	68.8022
SF$_6$		51.55	51.85	0.3	0.0619	0.972	60	0.8	0.375	70.3575	75	68.2575
SiO$_2$		74.2	75	0.8	0.0793	0.9686	160	2.05	0.3902	71.8595	78.0488	69.4088

Presents data on the performance of various coupling substrates in achieving enhanced angular sensitivity, FOM, DA, QF, and CSF. The symbol [bold] reflected inside Table [3] represents the results for a specific layer, which was found to be the most effective coupling substrate amongst the ones discussed
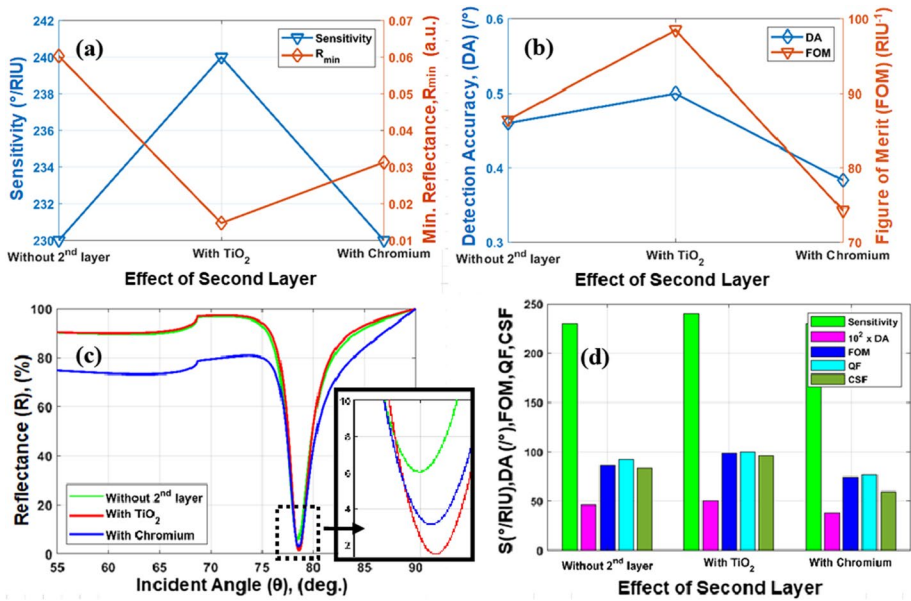
Fig. 4 **a** Angular sensitivity and minimum reflectance (R_{min}), **b** DA and FOM, **c** Reflectance intensity and incident angle, and **d** Overall performance of SPR sensor for different adhesion (second) layer, considering at sensing layer refractive index, n_s of 1.3348

4.4 Effect of fourth layer on sensing performance (CaF$_2$/ TiO$_2$/Ag/2D-TMDC/ Analyte—1.3348)

In the fourth layer, two-dimensional (2D) transition metal dichalcogenides (TMDs) materials (BP, Graphene, PtSe$_2$ MoS$_2$, MoSe$_2$, WS$_2$, WSe$_2$) have been investigated to increase the sensitivity of the proposed sensor. Therefore, the each of BP, Graphene, PtSe$_2$, MoS$_2$, MoSe$_2$, WS$_2$, and WSe$_2$ materials have been analyzed as well as their number of layers to find the best sensor performance. All the obtained measurement results are tabulated in Table 6 and plotted in Fig. 6. By the comparison of each numerical result, it is found that BP having three-layer shows the highest sensitivity in comparison with Graphene, PtSe$_2$ MoS$_2$, MoSe$_2$, WS$_2$, and WSe$_2$ as the fourth layer. In Fig. 6a, it is found that three-layer BP has the maximum sensitivity and minimum reflectance intensity, as well as the DA, FOM, QF, and CSF of the BP layer is the most raised value compared to other 2D TMDs materials, as shown in Fig. 6b–d.

4.5 Effect of fifth layer on sensing performance (CaF$_2$/ TiO$_2$/Ag/BP*3L/2D-TMDC/ Analyte—1.3348)

For further sensor parameter increment, a 2D TMDC layer is added on top of the BP layer to increase the sensitivity of the proposed sensor. From the numerical analysis results data tabulated in Table 7, from which it can be found that the highest sensitivity is obtained for the graphene monolayer as a fifth layer. Considering all the 2D-TMDC materials MoS$_2$,

Table 4 Comparison of various second adhesion layer materials for various sensor parameters

Prism	2nd Layer	Metal/Analyte	θ_1	θ_2	$\Delta\theta_{SPR}$	R_{min}	R_{max}	Sensitivity (S)	FWHM	DA	FOM	QF	CSF
CaF_2	No-layer	Ag/Analyte,$\Delta n = \|1.3348 - 1.3398\| = 0.005$	78.5	79.65	1.15	0.0603	0.9683	230	2.5	0.46	86.4524	92	83.54
	TiO$_2$		**78.6**	**79.8**	**1.2**	**0.0147**	**0.9728**	**240**	**2.4**	**0.5**	**98.53**	**100**	**95.81**
	Chromium		78.6	79.75	1.15	0.0313	0.8093	230	3	0.38	74.267	76.67	59.65

Presents data on the performance of various coupling substrates in achieving enhanced angular sensitivity, FOM, DA, QF, and CSF. The symbol [bold] reflected inside Table [4] represents the results for a specific layer, which was found to be the most effective coupling substrate amongst the ones discussed
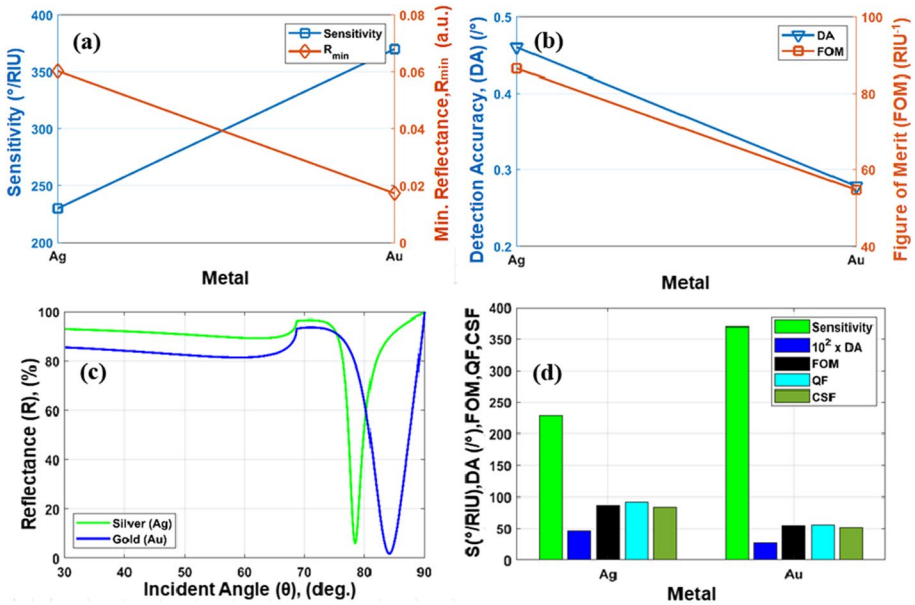
Fig. 5 **a** Angular sensitivity and minimum reflectance (R_{min}), **b** DA and FOM, **c** Reflectance intensity and incident angle, and **d** Overall performance of SPR sensor for different plasmonic metal (third) layer, considering at sensing layer refractive index, n_s of 1.3348

$MoSe_2$, WS_2, WSe_2, Mxene, and graphene, the graphene shows the utmost performance as illustrated in Fig. 7a–d.

4.6 Effect of analyte on sensing performance

The sensitivity of the proposed SPR has been improved (from 250 °/RIU to 390 °/RIU), corresponding to the RI of the sensing medium (range from 1.3348 to 1.3398), as depicted in Fig. 8a. The DA and FOM increase from 0.118 to 0.438 and from 55.60/RIU to 75.93/RIU, respectively, as shown in Fig. 8b. Eventually, the proposed sensor is able to provide a maximum sensitivity value of 390 °/RIU, which can be used for detecting the SARS-CoV-2 virus. Moreover, the SPR curve characteristics ($\Delta\theta_{SPR}$) are assessed with the varied RI (range from 1.3348 to 1.3398) for the different heterostructure SPR sensor model configuration of (i) CaF_2/Ag/Sensing-Layer, (ii) CaF_2/TiO_2/Ag/-Sensing-Layer, (iii) CaF_2/TiO_2/Ag/BP*3L/Sensing-Layer, and (iv) CaF_2/TiO_2/Ag/BP*3L/Graphene*1L/Sensing-Layer as shown in Fig. 9a–d, respectively. From the plot, it is observed that the resonance angle change increases on the additional layers from SPR angle shift 1.15 deg to SPR angle shift 1.95 deg which contributes to the increment of the angular sensitivity for the analyte refractive index range.

Table 5 Comparison of various third-layer plasmonic materials for various sensor parameters

Prism	2nd layer	Metal	Analyte	θ_1	θ_2	$\Delta\theta_{SPR}$	R_{min}	R_{max}	Sensitivity (S) deg/RIU	FWHM	DA	FOM	QF	CSF
CaF$_2$	TiO$_2$	**Ag**	$\Delta n = \lvert 1.3348 - 1.3398 \rvert = 0.005$	**78.6**	**79.8**	**1.2**	**0.0147**	**0.9728**	**240**	**2.4**	**0.5**	**98.53**	**100**	**95.81**
	TIO$_2$	Au		84.15	86	1.85	0.0173	0.9394	370	6.65	0.278	54.67654	55.6391	51.304812

Presents data on the performance of various coupling substrates in achieving enhanced angular sensitivity, FOM, DA, QF, and CSF. The symbol [bold] reflected inside Table [5] represents the results for a specific layer, which was found to be the most effective coupling substrate amongst the ones discussed

Table 6 Comparison of various Fourth layer CaF$_2$/ TiO$_2$/Ag/2D-TMDC/Analyte structures for various sensor parameters of analyte $\Delta n = |1.3348 - 1.3398|$

4th Layer—2D TMDC (mon-olayer×L)	θ$_2$	θ$_1$	Δθ$_{SPR}$	R$_{min}$	R$_{max}$	Sensitivity (S)	FWHM	DA	FOM	QF	CSF
BP (0.53 nm ×1)	80.9	79.6	1.3	0.008	0.9729	260	2.65	0.491	97.33	98.11	94.67
BP (0.53 nm ×3)	*83.85*	*82.05*	*1.8*	*0.00037*	*0.9727*	*360*	*3.475*	*0.518*	*103.6*	*103.6*	*100.7*
BP (0.53 nm ×5)	87.4	86.05	1.35	0.1193	0.9728	270	4.35	0.31	54.66	62.07	52.98
PtSe2 (2 nm)	**83.45**	**81.85**	**1.6**	**0.2375**	**0.9679**	**320**	**4.5**	**0.356**	**54.22**	**71.11**	**51.94**
PtSe2 (4 nm)	83.95	83.55	0.4	0.6881	0.9656	80	8.4	0.048	2.97	9.524	2.643
PtSe2 (6 nm)	82.45	82.3	0.15	0.8405	0.9644	30	9.5	0.016	0.504	3.158	0.391
MoS2 (0.65 nm ×1)	**81.95**	**80.5**	**1.45**	**0.0828**	**0.9704**	**290**	**4.05**	**0.358**	**65.68**	**71.6**	**63.56**
MoS2 (0.65 nm ×3)	84.85	84.4	0.45	0.6039	0.9688	90	7.35	0.061	4.85	12.24	4.468
MoS2 (0.65 nm ×5)	83.3	83.2	0.1	0.8599	0.9681	20	8.15	0.012	0.344	2.454	0.266
MoSe2 (0.70 nm ×1)	**81.85**	**80.45**	**1.4**	**0.0625**	**0.9706**	**280**	**3.9**	**0.359**	**67.31**	**71.79**	**65.2**
MoSe2 (0.70 nm ×3)	85.1	84.55	0.55	0.5553	0.9688	110	7.65	0.072	6.394	14.38	5.946
MoSe2 (0.70 nm ×5)	83.65	83.55	0.1	0.8543	0.968	20	9.05	0.011	0.322	2.21	0.251
WS2 (0.80 nm ×1)	**82.6**	**81.05**	**1.55**	**0.0113**	**0.9716**	**310**	**3.65**	**0.425**	**83.97**	**84.93**	**81.56**
WS2 (0.80 nm ×3)	85.9	85.4	0.5	0.784	0.9703	100	6.85	0.073	3.153	14.6	2.72
WS2 (0.80 nm ×5)	82.7	82.2	0.5	0.9494	0.9696	100	7.6	0.066	0.666	13.16	0.266
WSe2 (0.70 nm ×1)	**81.9**	**80.45**	**1.45**	**0.01**	**0.9714**	**290**	**3.5**	**0.414**	**82.03**	**82.86**	**79.66**
WSe2 (0.70 nm ×3)	86.15	85.8	0.35	0.4553	0.97	70	6.2	0.056	6.15	11.29	5.811
WSe2 (0.70 nm ×5)	84.3	83.9	0.4	0.9012	0.9692	80	8.15	0.049	0.97	9.816	0.667
Graphene (0.34 nm ×1)	80.35	79.1	1.25	0.0031	0.9709	250	3	0.417	83.08	83.33	80.65
Graphene (0.34 nm ×3)	**81.55**	**80.2**	**1.35**	**0.0943**	**0.9691**	**270**	**3.9**	**0.346**	**62.7**	**69.23**	**60.56**
Graphene (0.34 nm ×5)	82.85	81.35	1.5	0.2341	0.968	300	4.4	0.341	52.22	68.18	50.04

Presents data on the performance of various coupling substrates in achieving enhanced angular sensitivity, FOM, DA, QF, and CSF. The symbol [bold] reflected inside Table [6] represents the results for a specific layer, which was found to be the most effective coupling substrate amongst the ones discussed
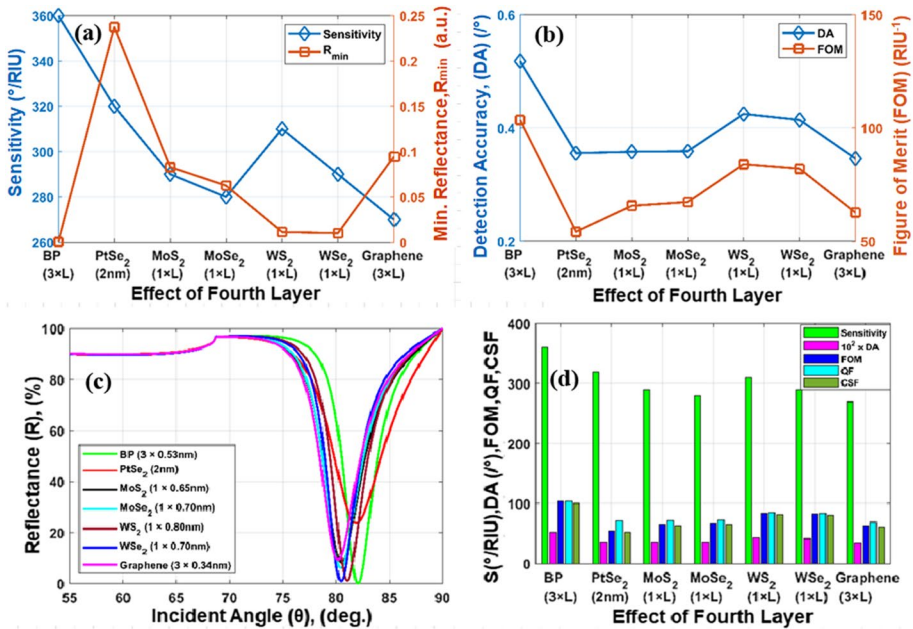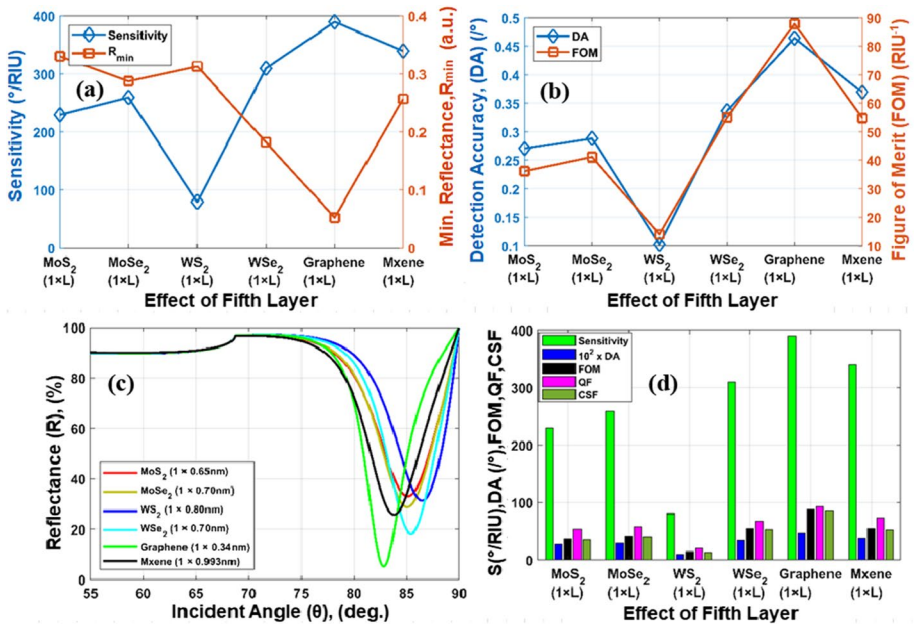
Fig. 6 **a** angular sensitivity and minimum reflectance (R_{min}), **b** DA and FOM, **c** Reflectance intensity and incident angle, and **d** Overall performance of SPR sensor for different 2D (fourth) material, considering at sensing layer refractive index, n_s of 1.3348

4.7 Electric field analysis

The electric field intensity approaches its maximum value when the reflectance curve shows the minimum value of reflectivity. It is one of the crucial elements for detecting the target analyte on the sensor surface (Mostufa et al. 2022b) and for the proposed configuration the intensified electric field is obtained. The electric field intensity and angle of incidence as a function of normal distance from the interface for each respective structure of SPR sensor have been plotted in Fig. 10. In comparison to other structures, it is found that the proposed sensor electric field intensity has more ability to strike the metal surface's free electrons in the surface plasmon polaritons (SPPs) mode, which enhances the sensitivity and FOM. In addition, the added 2D TMDC materials over the plasmonic metal layer enhance the electric field intensity, which enhances the sensitivity by increasing the mobility of electrons. Figure 10a–d represents the behavior of the electric field intensity for the CaF_2/Ag/Analyte, CaF_2/TiO_2/Ag/Analyte, CaF_2/TiO_2/Ag/BP*3L/-Analyte, and CaF_2/TiO_2/Ag/BP*3L/Graphene*1L/Analyte structures respectively.

To ensure top-notch results from SPR biosensors, the analysis of loss profiles is crucial. These biosensors detect target biomolecules by utilizing the light absorbed by the metallic nanoparticle-coated sensing layer. To minimize loss and improve performance, several approaches can be employed, such as increasing the refractive index (RI) of the sensing layer, adjusting its thickness, choosing an appropriate metal, selecting an appropriate wavelength range and angle of incidence, applying anti-reflection coatings on the surfaces of the sensor, and adding a protective layer. In the proposed sensor, CaF_2 is favored as a material that has demonstrated promise in this area due to its high light

Table 7 Comparison of various Fourth layer CaF$_2$/ TiO$_2$/Ag/Ag/BP*3L/2D-TMDC/Analyte structures for various sensor parameters $\Delta n = |1.3348 - 1.3398|$

5th Layer	θ_2	θ_1	$\Delta\theta_{SPR}$	R_{min}	R_{max}	S	FWHM	DA	FOM	QF	CSF
MoS2 (0.65 nm×1)	86.25	85.1	1.15	0.3306	0.9701	230	4.25	0.271	36.23	54.12	34.61
MoSe2 (0.70 nm×1)	86.35	85.05	1.3	0.2877	0.9702	260	4.5	0.289	41.16	57.78	39.43
WS2 (0.80 nm×1)	86.85	86.45	0.4	0.3131	0.9716	80	3.9	0.103	14.09	20.51	13.51
WSe2 (0.70 nm×1)	86.95	85.4	1.55	0.1827	0.9714	310	4.6	0.337	55.08	67.39	53.15
Graphene (0.34 nm×1)	**84.8**	**82.85**	**1.95**	**0.0528**	**0.9712**	**390**	**4.2**	**0.464**	**87.95**	**92.86**	**85.28**
Graphene (0.34 nm×2)	85.6	83.65	1.95	0.1578	0.9698	390	4.65	0.419	70.64	83.87	68.1
Graphene (0.34 nm×3)	85.95	84.4	1.55	0.288	0.969	310	4.5	0.344	49.05	68.89	46.91
Mxene (0.993 nm×1)	85.5	83.8	1.7	0.2575	0.9682	340	4.6	0.37	54.88	73.91	52.53

Presents data on the performance of various coupling substrates in achieving enhanced angular sensitivity, FOM, DA, QF, and CSF. The symbol [bold] reflected inside Table [7] represents the results for a specific layer, which was found to be the most effective coupling substrate amongst the ones discussed

Fig. 7 **a** angular sensitivity and minimum reflectance (R_{min}), **b** DA and FOM, **c** Reflectance intensity and incident angle, and **d** Overall performance of SPR sensor for different 2D TMDs (fifth) material, considering at sensing layer refractive index, n_s of 1.3348
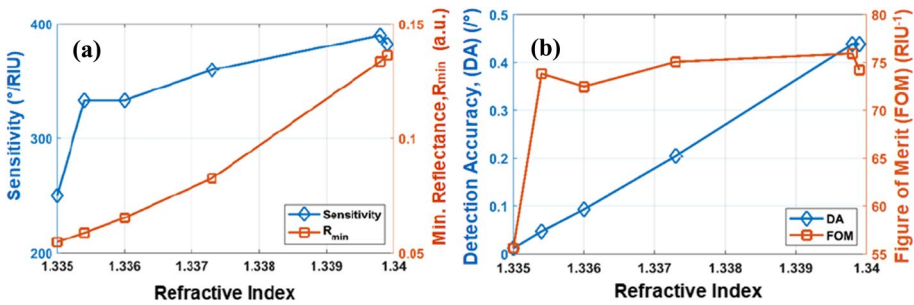
Fig. 8 **a** Sensitivity and R_{min}, and **b** DA and FOM respected to refractive index (n_s) of the sensing layer, considering n_s of 1.3348 + Δn (Here, $\Delta n = 0.005$)

transmission, reduced Fresnel loss, small dispersion, and low temperature dependence of its refractive index (Malitson 1963; Saad 2009; Yadav and Jain 2016). Furthermore, FDTD simulation provides information on light absorption and scattering in the sensor by simulating its electric and magnetic fields, which can be used to calculate the loss profile.

Finally, the output results are compared with some recently reported work and structure (year from 2018 to 2022) as tabulated in Table 8. From the comparison Table 8, it can be obtained that the resultant sensitivity of the proposed sensor is highest comparing all the
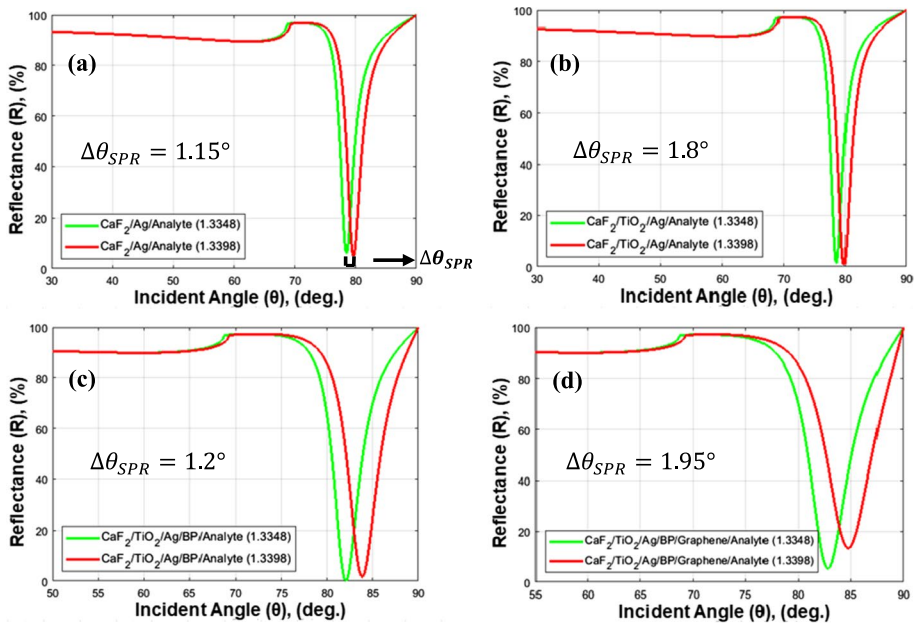
Fig. 9 Effect of each layer on the increment of the sensitivity structure: **a** CaF$_2$/Ag/Analyte, **b** CaF$_2$/TiO$_2$/Ag/Analyte, and **c** CaF$_2$/TiO$_2$/Ag /BP*3L/Analyte **d** CaF$_2$/TiO$_2$/Ag/BP*3L/Graphene*1L/Analyte for analyte change (1.3348–1.3398)

sensor parameters. So, this proposed sensor is highly optimized and exhibits the highest sensor parameters which are very crucial for biological analyte detection.

5 Target analytes for detection of SARS-CoV-2 virus

To detect the SARS-CoV-2 virus, it's essential to extract the virus RNA. The reverse transcription polymerase chain reaction (RT-PCR) is the most commonly used technique to extract the RNA sequence for the SARS-CoV-2 virus. However, the RT-PCR technique is a long-time process (required ~ 4 h) to extract the RNA. To overcome this process, Wang et al. (2020) established a subsequent RT-PCR technique known as the pcMNPs technique for RNA extraction (required ~ 30 min). Generally, the SPR sensor surface is immobilized with specific probe RNA sequences to detect the specific RNA sequences. Theoretically, the SPR sensor is proposed to detect the SARS-CoV-2 virus, whereas, the sensor surface can be immobilized with specific probe sequences to detect the SARS-CoV-2 virus RNA sequence. It's possible to detect the different variants of the SARS-CoV-2 virus by the proposed sensor with specific probe ligands. In Table 9, primers and probe genome sequences are specified for the detection of different variants of the SARS-CoV-2 virus (Wee et al. 2020; Xu et al. 2020; Li et al. 2020). In addition, the entirely matching (mr) sequence and mismatching (wt) sequence with probe (sh) linker is tabulated. A specimen is considered COVID-19 test result is positive only if the target analytes (ins214EPE, L452R, and del69-70) are detected by the proposed SPR sensor. To detect the SARS-CoV-2 virus, it's essential to extract the virus RNA. The reverse transcription polymerase chain

Fig. 10 Electric field intensity and two-dimensional plots of electric field distribution for heterostructure ▶ SPR sensor model of **a** Three layer—CaF$_2$/Ag/Analyte, **b** Four layer—CaF$_2$/TiO$_2$/Ag/Analyte, **c** Five layer—CaF$_2$/TiO$_2$/Ag/BP*3L/Analyte, and **d** Six layer—CaF$_2$/TiO$_2$/Ag/BP*3L/Graphene*1L/Analyte configuration

reaction (RT-PCR) is the most commonly used technique to extract the RNA sequence for the SARS-CoV-2 virus. However, the RT-PCR technique is a long-time process (required ~ 4 h) to extract the RNA. To overcome this process, Wang et al. (2020) established a subsequent RT-PCR technique known as the pcMNPs technique for RNA extraction (required ~ 30 min). Generally, the SPR sensor surface is immobilized with specific probe RNA sequences to detect the specific RNA sequences. Theoretically, the SPR sensor is proposed to detect the SARS-CoV-2 virus, whereas, the sensor surface can be immobilized with specific probe sequences to detect the SARS-CoV-2 virus RNA sequence. It's possible to detect the different variants of the SARS-CoV-2 virus by the proposed sensor with specific probe ligands. In Table 9, primers and probe genome sequences are specified for the detection of different variants of the SARS-CoV-2 virus (Wee et al. 2020; Xu et al. 2020; Li et al. 2020). In addition, the entirely matching (mr) sequence and mismatching (wt) sequence with probe (sh) linker is tabulated. A specimen is considered COVID-19 test result is positive only if the target analytes (ins214EPE, L452R, and del69-70) are detected by the proposed SPR sensor.

There are various approaches available for detecting the COVID-19 virus. Table 10 displays the most commonly used test types for identifying the presence of the coronavirus.

6 Real-time detection of target analytes

To detect the analytes, the specified probe ligands are generally immobilized onto the sensor surface. The analyte flows onto the sensor surface through the phosphate buffer solution (PBS) as an effective viral transport medium. The refractive index (RI) of the sensing layer is changed with the immobilization of ligand analytes. In the simulation, the sensor surface RI (n$_s$)is1.3348 + Δn; where the RI of PBS (pH-7.4) is 1.3348 and Δn is fluctuating owing to the immobilization of different concentrations of ligand-analyte. The change in refractive index (Δn) can be computed as (Mostufa et al. 2022; Mudgal et al. 2020; Diéguez et al. 2009; Cennamo et al. 2013),Δn = c$_a$(dn/dc), where c$_a$ represents the concentration of the target analyte, and dn/dc indicates the change in RI as the analyte concentration changes. Numerous studies in the literature, the refractive index increment parameters dn/dc values for proteins (Peng et al. 2020; Ball and Ramsden 1998) range from 0.186 ± 0.002 cm^3/g, for DNA (Tumolo et al. 2004; Patel et al. 2017) from 0.183 ± 0.006 cm^3/g, for RNA (Tumolo et al. 2004; Patel et al. 2017) from 0.17 to 0.19 cm^3/g and for SARS-CoV-2 RNA (Mostufa et al. 2022; Moznuzzaman et al. 2021) 0.181 cm^3/g. In this article, the proposed sensor is numerically studied with different concentrations of analytes. Figure 11 shows a linear response between different concentrations (ranging from 0 to 1000 nM) of target analytes and sensing region RI for monitoring binding interactions between ligands and analytes. The linear response can be described by an equation,$y = 5.1208e^{-6}x + 1.3348$, where the RI of PBS is 1.3348., (Moznuzzaman et al. 2021) 0.181 cm^3/g. In this article, the proposed sensor is numerically studied with different concentrations of analytes. Figure 11 shows a linear response between different concentrations (ranging from 0 to 1000 nM) of target analytes and sensing region RI for monitoring binding interactions between ligands and

Electric field intensity vs. distance (nm)　　　　Angle of incidence vs. distance (nm)
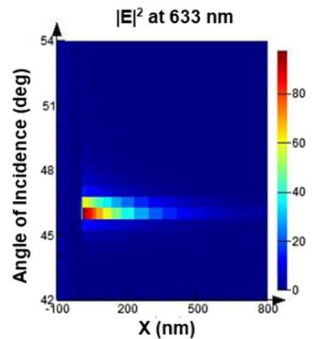
(a)

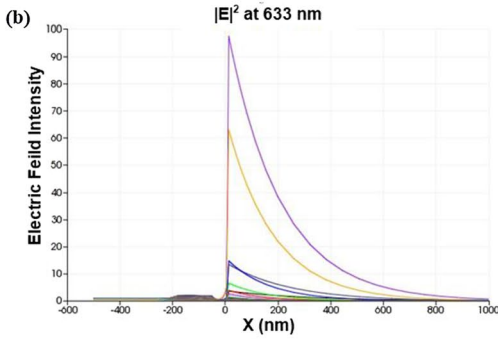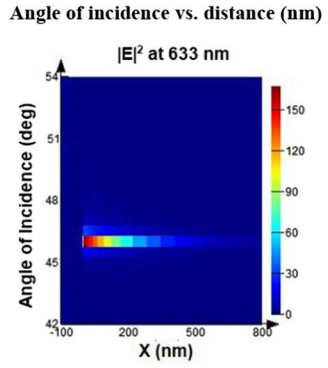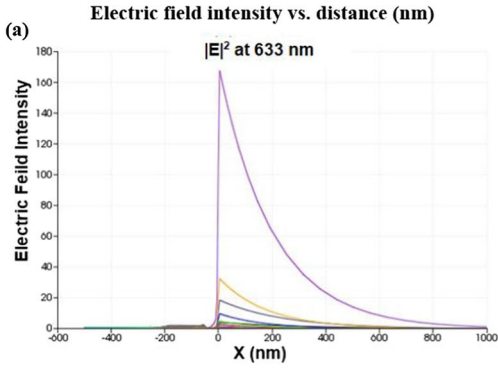(b)

(c)

(d)
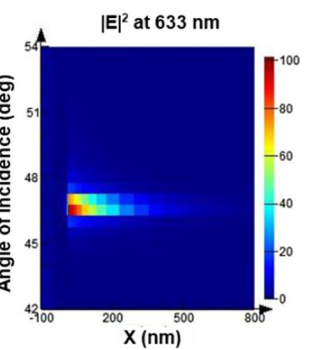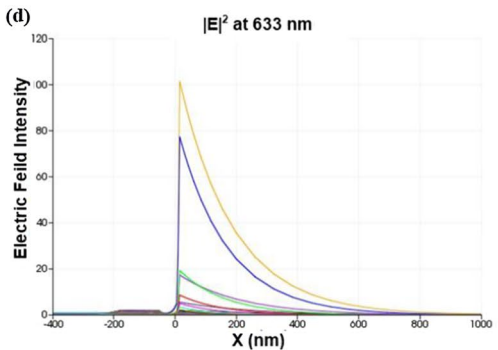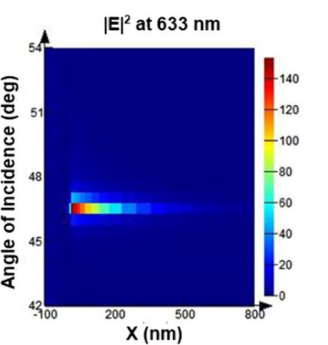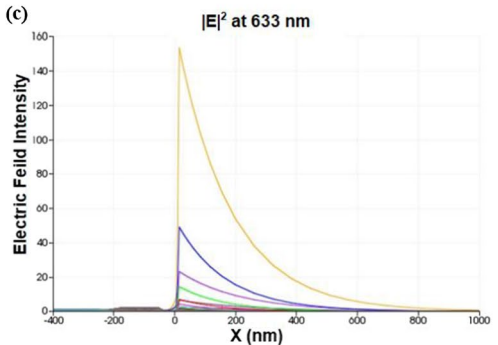
Table 8 Performance comparison with some recently reported structures

References	Reported Year	Structure	Sensitivity [Deg/RIU]	DA	FOM	Q-factor [RIU^{-1}]
Park et al. (2012)	2018	SF$_6$/Chromium/Au/BP/MoS$_2$	79.27	–	46.25	46.58
Park et al. (2012)	2018	SF$_6$/Chromium/Au/BP	81.10	–	21.51	68.60
Park et al. (2012)	2018	SF$_6$/Chromium/Au/BP/MoSe$_2$	82.92	–	39.04	49.05
Park et al. (2012)	2018	SF$_6$/Chromium/Au/BP/Graphene	85.97	–	27.04	55.81
Rahman et al. (2017)	2017	SF$_{10}$/Au/MoS$_2$/Graphene	87.80	1.28	–	17.56
Rikta et al. (2021)	2021	SF$_{10}$/Au/α-SnSe$_2$/Phosphorene	96.43	–	12.36	–
Moznuzzaman et al. (2020)	2020	SF$_{11}$/Ag/graphene/MoS$_2$/TiO$_2$/SiO$_2$	98	0.88	–	88.88
Kushwaha et al. (2018)	2018	SF$_{10}$/ZnO/Au/MoS$_2$/Graphene	101.58	1.81	–	15.11
Park et al. (2012)	2018	SF$_6$/Chromium/Au/BP/WSe$_2$	104.27	–	31.91	63.59
Park et al. (2012)	2018	SF$_6$/Chromium/Au/BP/WS$_2$	105.49	–	31.50	66.25
Hossain et al. (2020)	2020	SF$_{11}$/Au/MoS$_2$/Graphene	130	–	17.02	–
Lin et al. (2020)	2020	SF$_{11}$/Au/MoS$_2$/WS$_2$/WSe$_2$	142	–	–	–
Jia et al. (2019)	2020	Prism/Ag/PtSe$_2$	162	–	14.93	–
Jia et al. (2019)	2020	Prism/Au/PtSe$_2$	165	–	14.12	–
Nurrohman and Chiu (2020)	2020	BK$_7$/Au/WSe$_2$/Graphene	178.87	–	27.86	–
Maurya et al. (2015b)	2015	Prism/Au/BP	180	–	–	–
Akib et al. (2021)	2021	Bk$_7$/Au/PtSe$_2$/Graphene/PBS	183.3	1.41	47.00	–
Rahman et al. (2020)	2018	Prism/Au/PtSe$_2$/WS$_2$	187	–	15.72	29.39
Park et al. (2012)	2018	SF$_6$/Chromium/Au/BP/WS$_2$	187	–	–	–
Rahman et al. (2020)	2020	Prism/Ag/PtSe$_2$/WS$_2$	194	–	17.64	34.22
Rahman et al. (2021)	2022	BK$_7$/Au/WSe$_2$/PtSe$_2$/BP	200	0.088	17.70	–
Kumar et al. (2021)	2021	BK$_7$/ZnO/Si/MXene/Sensing layer	231	0.17	–	39.83
Kumar et al. (2020)	2020	BK$_7$/ZnO/Ag/BaTiO$_3$/WS$_2$	235	1.27	–	63.51
Panda and Pukhrambam (2021)	2021	CaF$_2$/TiO$_2$/Ag/PtSe$_2$/WS$_2$	240.10	1.99	–	78.46
Jia et al. (2022)	2022	BK$_7$/Au/GeS	260	0.143	33.4	–
Kumar et al. (2022)	2022	SiO$_2$/Au/Ga-doped ZnO/MXene	264.59	0.115	30.48	–
Jia et al. (2022)	2022	BK$_7$/Ag/GeS	295	0.224	66.2	–

Table 8 (continued)

References	Reported Year	Structure	Sensitivity [Deg/RIU]	DA	FOM	Q-factor [RIU^{-1}]
Jia et al. (2022)	2022	BK$_7$/Al/GeS	320	0.294	1088.4	–
Yesudasu and Pradhan (2021)	2021	Prism/Ag/AlAs/TlBr/BP	475	–	79.72	80.37
Karki et al. (2022a)	2022	BK$_7$/Ag$_l$/MXene /Ag$_2$/ZnO/ graphene	161	0.4219	–	67.93
Uniyal et al. (2022a)	2022	Ag/InP/graphene	506	0.144	–	72.86
Uniyal et al. (2022b)	2022	BK7 prism/cytop/Ag/PtSe$_2$	229–384	0.32	115.2	–
Karki et al. (2022b)	2022	Ag/Zinc sulfide/silicon dioxide/black phosphorus	664.6	–	–	200
Mudgal et al. (2022)	2022	Ag/Si$_3$N$_4$	6287 nm/RIU	–	–	873.19
Karki et al. (2022c)	2022	Prism/Ag/MXene/ZnO/Graphene	136.5	–	–	38.7
Proposed	**2022**	**CaF$_2$/TiO$_2$/Ag/BP/Graphene**	**390**	**0.464**	**87.95**	**92.86**

Presents data on the performance of various coupling substrates in achieving enhanced angular sensitivity, FOM, DA, QF, and CSF. The symbol [bold] reflected inside Table [8] represents the results for a specific layer, which was found to be the most effective coupling substrate amongst the ones discussed

Table 9 Primers and probes sequence alignment for diagnoses of the different SARS-CoV-2 virus variants

Variants – Target Spike Genes	Primers & Probes	Sequences (5'–3')	References
Omicron (B.1.1.529) – ins214EPE	S-ins214EPE-fwd	GAA AAC AGG GTA ATT TCA AAA ATC TTA GGG	Phan et al. (2022), Yolshin et al. (2021), Peacock et al. (2022), Nörz et al. (2021)
	S-ins214EPE-rev	CCT ATT GGC AAA TCT ACC AAT GGT TCT AA	
	S-ins214EPE-probe	56-FAM/TA TAG TGC G/ZEN/T **GAG CCA GAA GAT CTC CCT** /3IABkFQ	
	S-ins214EPE-mr	**AGG GAG ATC TTC TGG CTC**	
	S-ins214EPE-wt	AGG GGC TCT *TTA* AGG C<u>CT</u>	
Delta (B.1.617.2) – L452R	S-L452R- fwd	GAT T(+C)T AAG GTT GGT GG(2OMe-U) AAT	Nörz et al. (2021), Hamill et al. (2022)
	S-L452R- rev	TTT CAG TTG AAA TAT CT(+C) TC(2OMe-U) C	
	S-L452R- probe	Atto425- T(+T)A C(+C)(+G) (+G)**TA TAG ATT** (+G)**TT** TA(+G) - BHQ1	
	S-L452R- mr	AA(+C) **AAT CTA TA**(+C)	
	S-L452R- wt	A**T**(+C) AAC TCA **TA**(+C)	
Alpha (B.1.1.7) – del69-70	S-del69-70-fwd	GTT TTA CAT TCA ACT CAG GAC TTG TTC T	Phan et al. (2022), Yolshin et al. (2021)
	S-del69-70-rev	CAT CAT TAA ATG GTA GGA CAG GGT TAT C	
	S-del69-70-probe	56-FAM/TC CAT GTT A/ZEN/T **CTC TGG GAC CAA TGG TAC** /3IABkFQ	
	S-del69-70-mr	**GTA CCA TTG GTC CCA GAG**	
	S-del69-70-wt	**GT**T CAT *TTA* TCA TTA **GAG**	

Table 10 Common test types for the detection of coronavirus

S/N	Test Type	Explanation
01	RT-PCR Test	The RT-PCR test is the most commonly used method for detecting the RNA of the virus, which is its genetic material
02	Antigen Test	Antigen tests quickly detect proteins found on the surface of the virus, but they are not as accurate as RT-PCR tests. However, they give results much quicker
03	Antibody Test	Antibody tests look for antibodies generated by the immune system in response to a SARS-CoV-2 infection, but they cannot identify an ongoing infection. They only show if the person has been exposed to the virus in the past

Fig. 11 Schematic diagram of a linear relationship between the different concentrations of target analytes and the sensing layer refractive index of the proposed sensor
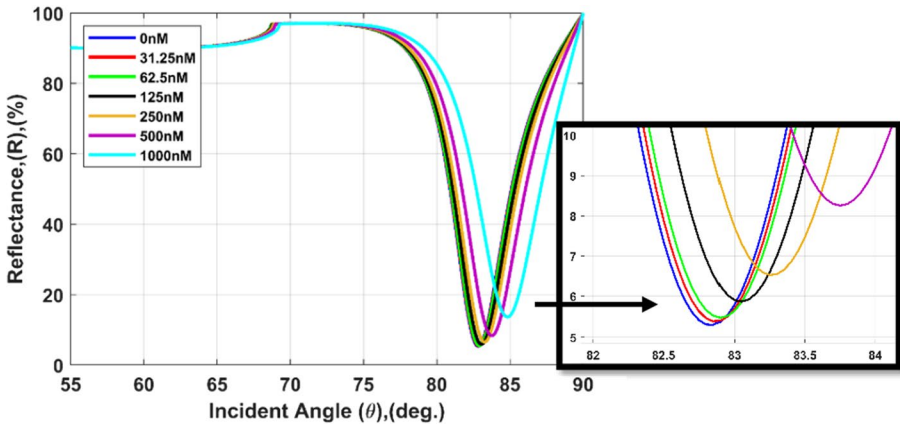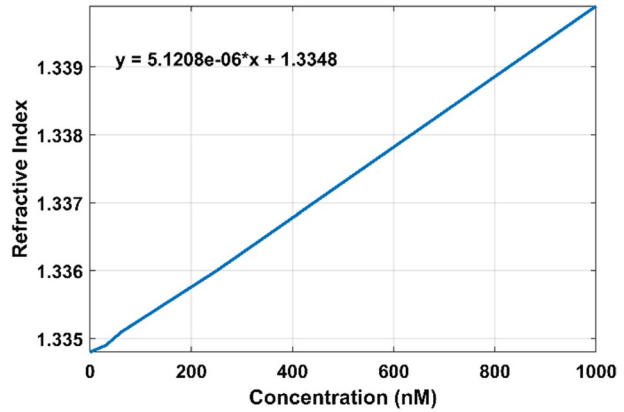
Fig. 12 Schematic diagram of SPR curve characteristics of the proposed sensor for different concentrated (0–1000 nM) levels of biomolecules absorbing for diagnosis of target analytes

analytes. The linear response can be described by an equation, $y = 5.1208e^{-6}x + 1.3348$, where the RI of PBS is 1.3348.

Figure 12 shows SPR angle is shifted rightwards with the variation of different concentrated analytes. Moreover, the attributors' shifting parameters are tabulated in Table 11.

In Table 10, shows the sensor performance and detection attributes for different concentrations of the analyte. In the simulation, without analytes, the sensor detects the minimum reflectance (R_{min}) is 0.0528, and the SPR angle (θ_1) is 82.85°. When the sensor probe ligand interacts with the mismatching type (wt) analyte, in this circumstance R_{min} is 0.0538, and θ_1 is 82.88°. The minimum reflectance is increased by 0.001 and the SPR angle shifted by 0.03°. Hereafter, when the probe ligand is immobilized with the entirely matching type (mr) analyte the R_{min} is 0.0547, and θ_1 is 82.90°. Conspicuously, the change of minimum reflectance (ΔR_{min}^{th}) is 0.0019 and the change in SPR angle ($\Delta \theta_{SPR}^{th}$) is 0.05°. Similarly, with the immobilization of target analytes in the sensing region, the refractive index (RI) of the sensing layer is incremented. As a result, detection attributes are shifted rightwards, otherwise, it's remained the same. Figure 11, shows the linear relationship between the different concentrations of target analytes and the sensing layer refractive index of the

Table 11 Diagnosis attributes for different concentrations of the target analyte

Configuration	Different Concentration (nM) of Analytes	Δn	Cumulative RI of Analyte	θ_1	$\Delta\theta_{SPR}$	R_{min}	ΔR_{min}	FWHM
CaF$_2$/TiO$_2$/Ag/BP/ Graphene	0 nM (probe)	–	1.3348	82.85	–	0.0528	–	4.20
	31.25 nM (wt)	0.0001	1.3349	82.88	0.03	0.0538	0.001	4.22
	62.5 nM (mr)	0.0002	1.3350	82.9	$\Delta\theta_{SPR}^{th} = 0.05$	0.0547	$\Delta R_{min}^{th} = 0.0019$	4.25
	125 nM (mr)	0.0003	1.3354	83.05	0.2	0.0587	0.0059	4.25
	250 nM (mr)	0.0006	1.3360	83.25	0.4	0.0653	0.0125	4.30
	500 nM (mr)	0.0013	1.3373	83.75	0.9	0.0826	0.0298	4.40
	1000 nM (mr)	0.0026	1.3399	84.8	1.95	0.1363	0.0835	4.45

Pathology No	Circumstance	Result (COVID-19)
01	$\Delta R_{min}^{th} \le \Delta R_{min}^{Y} \& \Delta\theta_{SPR}^{th} \le \Delta\theta_{SPR}^{Y}$	Detected
02	$\Delta R_{min}^{th} > \Delta R_{min}^{Y} \& \Delta\theta_{SPR}^{th} > \Delta\theta_{SPR}^{Y}$	Not-Detected
03	$\Delta R_{min}^{th} \ge \Delta R_{min}^{Y} \& \Delta\theta_{SPR}^{th} \le \Delta\theta_{SPR}^{Y}$	Try again
04	$\Delta R_{min}^{th} \le \Delta R_{min}^{Y} \& \Delta\theta_{SPR}^{th} \ge \Delta\theta_{SPR}^{Y}$	Try again

Table 12 Detection result based on the attributes

*Different concentration of analytes, Y (0–1000 nM)

proposed sensor. For the detection of the target analytes ΔR_{min}^{th} and $\Delta\theta_{SPR}^{th}$ are calculated as follows in (24):

$$
\begin{bmatrix}
\Delta R_{min}^{th}[\%] = \left| R_{min}^{0\,nM} - R_{min}^{62.5\,nM} \right| = 0.19\% \\
\Delta\theta_{SPR}^{th}[\deg.] = \left| \theta_{SPR}^{0\,nM} - \theta_{SPR}^{62.5\,nM} \right| = 0.05 \text{ deg}
\end{bmatrix}
\tag{24}
$$

Eventually, $\mathbf{\Delta R_{min}^{th}}$ and $\mathbf{\Delta\theta_{SPR}^{th}}$ are the minimum threshold attributes for the detection of the target analytes. The detection of target analytes by the proposed sensor will be contingent on the conditions of the attributor characteristics of $\mathbf{\theta_{SPR} \sim R_{min}}$, tabulated in Table 12.

If the detection attributes $\mathbf{\Delta R_{min}^{Y} \sim \Delta\theta_{SPR}^{Y}}$ are larger or equivalent to $\mathbf{\Delta R_{min}^{th} \sim \Delta\theta_{SPR}^{th}}$ then the target analyte is detected. Similarly, If the $\mathbf{\Delta R_{min}^{Y} \sim \Delta\theta_{SPR}^{Y}}$ are smaller to $\mathbf{\Delta R_{min}^{th} \sim \Delta\theta_{SPR}^{th}}$ then the target analyte is not detected. In the numerical simulation, the proposed sensor performance is studied by the different concentrations of analytes and the sensor shows robust performance for detecting the target analytes.

7 Conclusion

The comparative and detailed examination of each prism, adhesions, metal, 2D, and TMDCs layer materials to identify the optimal sensor parameters was presented in this paper. It is generally known that the performance of SPR-based sensors varies depending on the sensor settings, and each parameter is essential for accurately detecting certain biomolecules. As a result of the above investigation, the obtained CaF2/TiO2/Ag/BP/Graphene/Sensing-layer SPR sensor structure has a maximum angular shift sensitivity of up to 390°/RIU, detection accuracy (DA) of 0.464, quality factor (QF) of 92.86/RIU, figure of merit (FOM) of 87.95, and combined sensitive factor (CSF) of 85.28. Later, this suggested structure was used to detect varied concentration (0–1000 nM) levels of biomolecule binding interactions between ligands and analytes for the diagnosis of SARS-CoV-2 target analytes. The proposed sensor is fully capable of detecting the various SARS-CoV-2 viral types. As a result, the actual application of the proposed sensor for medical and biological detection may open up new possibilities for quick label-free biological component identification.

Author contributions All authors contributed equally in preparing the manuscript.

Declarations

Competing interests The authors declare no conflict of interest.

References

Ahmadivand, A., Sinha, R., Kaya, S., Pala, N.: Rhodium plasmonics for deep-ultraviolet bio-chemical sensing. Plasmonics **11**, 839–849 (2016)

Akib, T.B.A., Mou, S.F., Rahman, M.M., Rana, M.M., Islam, M.R., Mehedi, I.M., Mahmud, M.P., Kouzani, A.Z.: Design and numerical analysis of a graphene-coated SPR biosensor for rapid detection of the novel coronavirus. Sensors **21**(10), 3491 (2021)

Alharbi, R., Irannejad, M., Yavuz, M.: A short review on the role of the metal-graphene hybrid nanostructure in promoting the localized surface plasmon resonance sensor performance. Sensors **19**(4), 862 (2019)

Artiles, M.S., Rout, C.S., Fisher, T.S.: Graphene-based hybrid materials and devices for biosensing. Adv. Drug Deliv. Rev. **63**(14–15), 1352–1360 (2011)

Astuti, I., Ysrafil: Severe Acute Respiratory Syndrome Coronavirus 2 (SARS-CoV-2): an overview of viral structure and host response. Diabetes Metab. Syndr. Clin. Res. Rev. 14(4), 407-412 (2020)

Ball, V., Ramsden, J.J.: Buffer dependence of refractive index increments of protein solutions. Biopolym. Orig. Res. Biomol. **46**(7), 489–492 (1998)

Bochenkov, V.E., Frederiksen, M., Sutherland, D.S.: Enhanced refractive index sensitivity of elevated short-range ordered nanohole arrays in optically thin plasmonic Au films. Opt. Express **21**(12), 14763–14770 (2013)

Campbell, C.T., Kim, G.: SPR microscopy and its applications to high-throughput analyses of biomolecular binding events and their kinetics. Biomaterials **28**(15), 2380–2392 (2007)

Cennamo, N., Massarotti, D., Galatus, R., Conte, L., Zeni, L.: Performance comparison of two sensors based on surface plasmon resonance in a plastic optical fiber. Sensors **13**(1), 721–735 (2013)

Chabot, V., Miron, Y., Grandbois, M., Charette, P.G.: Long range surface plasmon resonance for increased sensitivity in living cell biosensing through greater probing depth. Sens. Actuators B Chem. **174**, 94–101 (2012)

Chamoli, S.K., Singh, S.C., Guo, C.: 1-D metal-dielectric-metal grating structure as an ultra-narrowband perfect plasmonic absorber in the visible and its application in glucose detection. Plasmonics **15**, 1339–1350 (2020)

Chaudhary, V.S., Kumar, D., Kumar, S.: Gold-immobilized photonic crystal fiber-based SPR biosensor for detection of malaria disease in human body. IEEE Sens. J. **21**(16), 17800–17807 (2021)

Chen, R., Kan, L., Duan, F., He, L., Wang, M., Cui, J., Zhang, Z., Zhang, Z.: Surface plasmon resonance aptasensor based on niobium carbide MXene quantum dots for nucleocapsid of SARS-CoV-2 detection. Microchim. Acta **188**(10), 1–10 (2021)

Cho, E.: De moivre's formula for quaternions. Appl. Math. Lett. **11**(6), 33–35 (1998)

Dai, X., Liang, Y., Zhao, Y., Gan, S., Jia, Y., Xiang, Y.: Sensitivity enhancement of a surface plasmon resonance with tin selenide (SnSe) allotropes. Sensors **19**(1), 173 (2019)

Dey, B., Islam, M.S., Park, J.: Numerical design of high-performance WS2/metal/WS2/graphene heterostructure based surface plasmon resonance refractive index sensor. Results in Physics **23**, 104021 (2021)

Diéguez, L., Darwish, N., Mir, M., Martínez, E., Moreno, M., Samitier, J.: Effect of the refractive index of buffer solutions in evanescent optical biosensors. Sens. Lett. **7**(5), 851–855 (2009)

Douedi, S., Miskoff, J.: Novel coronavirus 2019 (COVID-19): a case report and review of treatments. Medicine **99**(19) (2020)

Englebienne, P., Van Hoonacker, A., Verhas, M.: Surface plasmon resonance: principles, methods and applications in biomedical sciences. Spectroscopy **17**(2–3), 255–273 (2003)

Eslami-Kaliji, F., Mirahmadi-Zare, S.Z., Nazem, S., Shafie, N., Ghaedi, R., Asadian-Esfahani, M.H.: A label-free SPR biosensor for specific detection of TLR4 expression; introducing of 10-HDA as an antagonist. Int. J. Biol. Macromol. **217**, 142–149 (2022)

Gan, S., Wang, H., Liang, J., Dai, X., Xiang, Y.: Ultra-sensitive refractive index sensors based on bloch surface waves with transition metal dichalcogenides. IEEE Sens. J. **19**(19), 8675–8680 (2019)

Guo, Y., Singh, N.M., Das, C.M., Ouyang, Q., Kang, L., Li, K., Coquet, P., Yong, K.T.: Two-dimensional PtSe2 theoretically enhanced Goos-Hänchen shift sensitive plasmonic biosensors. Plasmonics **15**(6), 1815–1826 (2020)

Hamill, V., Noll, L., Lu, N., Tsui, W.N.T., Porter, E.P., Gray, M., Sebhatu, T., Goerl, K., Brown, S., Palinski, R., Thomason, S.: Molecular detection of SARS-CoV-2 strains and differentiation of Delta variant strains. Transbound. Emerg. Dis. **69**(5), 2879–2889 (2022)

Hasib, M.H.H., Nur, J.N., Rizal, C., Shushama, K.N.: Improved transition metal dichalcogenides-based surface plasmon resonance biosensors. Condensed Matter **4**(2), 49 (2019)

Hassanpour, S.H., Nikbakht, J.: A comprehensive review on covid-19. Zahedan J. Res. Med. Sci. **23**(4), e109853 (2021)

Hossain, M.B., Kabir, M.A., Hossain, M.S., Ziaul Islam, K., Hossain, M.S., Pathan, M.I., Mondol, N., Abdulrazak, L.F., Hossain, M.A., Rana, M.M.: Numerical modeling of MoS2–graphene bilayer-based high-performance surface plasmon resonance sensor: structure optimization for DNA hybridization. Opt. Eng. **59**(10), 105105–105105 (2020)

Huang, Y., Yang, C., Xu, X.F., Xu, W., Liu, S.W.: Structural and functional properties of SARS-CoV-2 spike protein: potential antivirus drug development for COVID-19. Acta Pharmacol. Sin. **41**(9), 1141–1149 (2020)

Isaacs, S., Abdulhalim, I.: Long range surface plasmon resonance with ultra-high penetration depth for self-referenced sensing and ultra-low detection limit using diverging beam approach. Appl. Phys. Lett. **106**(19), 193701 (2015)

Jia, Y., Li, Z., Wang, H., Saeed, M., Cai, H.: Sensitivity enhancement of a surface plasmon resonance sensor with platinum diselenide. Sensors **20**(1), 131 (2019)

Jia, Y., Liao, Y., Cai, H.: Sensitivity improvement of surface plasmon resonance biosensors with GeS-metal layers. Electronics **11**(3), 332 (2022)

Karki, B., Vasudevan, B., Uniyal, A., Pal, A., Srivastava, V.: Hemoglobin detection in blood samples using a graphene-based surface plasmon resonance biosensor. Optik **270**, 169947 (2022a)

Karki, B., Trabelsi, Y., Uniyal, A., Pal, A.: Zinc sulfide, silicon dioxide, and black phosphorus based ultra-sensitive surface plasmon biosensor. Opt. Quant. Electron. **54**(2), 107 (2022b)

Karki, B., Jha, A., Pal, A., Srivastava, V.: Sensitivity enhancement of refractive index-based surface plasmon resonance sensor for glucose detection. Opt. Quant. Electron. **54**(9), 595 (2022c)

Katyal, J., Soni, R.K.: Localized surface plasmon resonance and refractive index sensitivity of metal–dielectric–metal multilayered nanostructures. Plasmonics **9**, 1171–1181 (2014)

Kitenge, D., Joshi, R.K., Hirai, M., Kumar, A.: Nanostructured silver films for surface plasmon resonance-based gas sensors. IEEE Sens. J. **9**(12), 1797–1801 (2009)

Kravets, V.G., Prorok, V.V., Poperenko, L.V., Shaykevich, I.A.: Ellipsometry and optical spectroscopy of low-dimensional family TMDs. Semicond. Phys. Quantum Electron. Optoelectron. **20**(3) (2017)

Kumar, A., Yadav, A.K., Kushwaha, A.S., Srivastava, S.K.: A comparative study among WS2, MoS2 and graphene based surface plasmon resonance (SPR) sensor. Sens. Actuators Rep. **2**(1), 100015 (2020)

Kumar, R., Pal, S., Prajapati, Y.K., Saini, J.P.: Sensitivity enhancement of MXene based SPR sensor using silicon: theoretical analysis. SILICON **13**, 1887–1894 (2021)

Kumar, R., Pal, S., Prajapati, Y.K., Kumar, S., Saini, J.P.: Sensitivity improvement of a MXene-immobilized SPR sensor with Ga-doped-ZnO for biomolecules detection. IEEE Sens. J. **22**(7), 6536–6543 (2022)

Kushwaha, A.S., Kumar, A., Kumar, R., Srivastava, S.K.: A study of surface plasmon resonance (SPR) based biosensor with improved sensitivity. Photon. Nanostruct. Fundam. Appl. **31**, 99–106 (2018)

Li, H.H.: Refractive index of alkali halides and its wavelength and temperature derivatives. J. Phys. Chem. Ref. Data **5**(2), 329–528 (1976)

Li, D., Zhang, J., Li, J.: Primer design for quantitative real-time PCR for the emerging Coronavirus SARS-CoV-2. Theranostics **10**(16), 7150 (2020)

Lial, M.L., Hornsby, J., Schneider, D.I., Daniels, C.: Trigonometry, 10th edn. Pearson, Boston (2012)

Lim, W.Y., Lan, B.L., Ramakrishnan, N.: Emerging biosensors to detect severe acute respiratory syndrome coronavirus 2 (SARS-CoV-2): a review. Biosensors **11**(11), 434 (2021)

Lin, Z., Chen, S., Lin, C.: Sensitivity improvement of a surface plasmon resonance sensor based on two-dimensional materials hybrid structure in visible region: a theoretical study. Sensors **20**(9), 2445 (2020)

Maddali, H., Miles, C.E., Kohn, J., O'Carroll, D.M.: Optical biosensors for virus detection: prospects for SARS-CoV-2/COVID-19. ChemBioChem **22**(7), 1176–1189 (2021)

Malitson, I.H.: A redetermination of some optical properties of calcium fluoride. Appl. Opt. **2**(11), 1103–1107 (1963)

Maurya, J.B., Prajapati, Y.K., Singh, V., Saini, J.P., Tripathi, R.: Performance of graphene–MoS 2 based surface plasmon resonance sensor using silicon layer. Opt. Quant. Electron. **47**, 3599–3611 (2015a)

Maurya, J.B., Prajapati, Y.K., Singh, V., Saini, J.P.: Sensitivity enhancement of surface plasmon resonance sensor based on graphene–MoS 2 hybrid structure with TiO 2–SiO 2 composite layer. Appl. Phys. A **121**, 525–533 (2015b)

Maurya, J.B., François, A., Prajapati, Y.K.: Two-dimensional layered nanomaterial-based one-dimensional photonic crystal refractive index sensor. Sensors **18**(3), 857 (2018)

Mostufa, S., Paul, A.K., Chakrabarti, K.: Detection of hemoglobin in blood and urine glucose level samples using a graphene-coated SPR based biosensor. OSA Continuum **4**(8), 2164–2176 (2021)

Mostufa, S., Akib, T.B.A., Rana, M.M., Mehedi, I.M., Al-Saggaf, U.M., Alsaggaf, A.U., Alsaggaf, M.U., Alam, M.S.: Numerical approach to design the graphene-based multilayered surface plasmon resonance biosensor for the rapid detection of the novel coronavirus. Opt. Continuum **1**(3), 494–515 (2022)

Mostufa, S., Akib, T.B.A., Rana, M.M., Mehedi, I.M., Al-Saggaf, U.M., Alsaggaf, A.U., Alsaggaf, M.U., Alam, M.S.: Numerical approach to design the graphene-based multilayered surface plasmon resonance biosensor for the rapid detection of the novel coronavirus. Opt. Continuum **1**(3), 494–515 (2022a)

Mostufa, S., Akib, T.B.A., Rana, M.M., Islam, M.R.: Highly sensitive TiO2/Au/graphene layer-based surface plasmon resonance biosensor for cancer detection. Biosensors **12**(8), 603 (2022b)

Moznuzzaman, M., Islam, M.R., Hossain, M.B., Mehedi, I.M.: Modeling of highly improved SPR sensor for formalin detection. Results Phys. **16**, 102874 (2020)

Moznuzzaman, M., Khan, I., Islam, M.R.: Nano-layered surface plasmon resonance-based highly sensitive biosensor for virus detection: a theoretical approach to detect SARS-CoV-2. AIP Adv. **11**(6), 065023 (2021)

Mudgal, N., Saharia, A., Agarwal, A., Ali, J., Yupapin, P., Singh, G.: Modeling of highly sensitive surface plasmon resonance (SPR) sensor for urine glucose detection. Opt. Quant. Electron. **52**, 1–14 (2020)

Mudgal, N., Saharia, A., Choure, K.K., Agarwal, A., Singh, G.: Sensitivity enhancement with anti-reflection coating of silicon nitride (Si3N4) layer in silver-based Surface Plasmon Resonance (SPR) sensor for sensing of DNA hybridization. Appl. Phys. A **126**(12), 946 (2020). https://doi.org/10.1007/s00339-020-04126-9

Mudgal, N., Choure, K.K., Falaswal, M.K., Pandey, R., Agarwal, A., Bhatia, D., Saharia, A., Sahu, S., Singh, G.: Impact of Taguchi optimization in fiber surface plasmon resonance sensors based on Si3N4 Layer. Braz. J. Phys. **52**(3), 80 (2022)

Nangare, S., Patil, P.: Black phosphorus nanostructure based highly sensitive and selective surface plasmon resonance sensor for biological and chemical sensing: a review. Crit. Rev. Anal. Chem. 1–26 (2021).

Nangare, S., Patil, P.: Black phosphorus nanostructure based highly sensitive and selective surface plasmon resonance sensor for biological and chemical sensing: a review. Crit. Rev. Anal. Chem. **53**(1), 1–26 (2023)

Nielsen, M.L., Blumenthal, D.J., Mork, J.: A transfer function approach to the small-signal response of saturated semiconductor optical amplifiers. J. Lightwave Technol. **18**(12), 2151–2157 (2000)

Nisha, A., Maheswari, P., Anbarasan, P.M., Rajesh, K.B., Jaroszewicz, Z.: Sensitivity enhancement of surface plasmon resonance sensor with 2D material covered noble and magnetic material (Ni). Opt. Quant. Electron. **51**, 1–12 (2019)

Nor, S.N.S., Rasanang, N.S., Karman, S., Zaman, W.S.W.K., Harun, S.W., Arof, H.: A Review: Surface Plasmon Resonance-Based Biosensor for Early Screening of SARS-CoV2 Infection. IEEE Access (2021)

Nörz, D., Grunwald, M., Tang, H.T., Olearo, F., Günther, T., Robitaille, A., Fischer, N., Grundhoff, A., Aepfelbacher, M., Pfefferle, S., Lütgehetmann, M.: Rapid automated screening for SARS-CoV-2 B. 1.617 lineage variants (Delta/Kappa) through a versatile toolset of QPCR-based SNP detection. Diagnostics **11**(10), 1818 (2021)

Nurrohman, D.T., Chiu, N.F.: Surface plasmon resonance biosensor performance analysis on 2D material based on graphene and transition metal dichalcogenides. ECS J. Solid State Sci. Technol. **9**(11), 115023 (2020)

Ouyang, Q., Zeng, S., Jiang, L., Hong, L., Xu, G., Dinh, X.Q., Qian, J., He, S., Qu, J., Coquet, P., Yong, K.T.: Sensitivity enhancement of transition metal dichalcogenides/silicon nanostructure-based surface plasmon resonance biosensor. Sci. Rep. **6**(1), 1–13 (2016)

Panda, A., Pukhrambam, P.D.: Modeling of high-performance SPR refractive index sensor employing novel 2D materials for detection of malaria pathogens. IEEE Trans. Nanobiosci. **21**(2), 312–319 (2021)

Pandey, P.S., Raghuwanshi, S.K., Shadab, A., Ansari, M.T.I., Tiwari, U.K., Kumar, S.: SPR based biosensing chip for COVID-19 diagnosis-A review. IEEE Sens. J. (2022)

Park, Y.L., Chen, B.R., Wood, R.J.: Design and fabrication of soft artificial skin using embedded microchannels and liquid conductors. IEEE Sens. J. **12**(8), 2711–2718 (2012)

Patel, T.R., Chojnowski, G., Koul, A., McKenna, S.A., Bujnicki, J.M.: Structural studies of RNA-protein complexes: a hybrid approach involving hydrodynamics, scattering, and computational methods. Methods **118**, 146–162 (2017)

Peacock, T.P., Brown, J.C., Zhou, J., Thakur, N., Newman, J., Kugathasan, R., Sukhova, K., Kaforou, M., Bailey, D., Barclay, W.S.: The SARS-CoV-2 variant, Omicron, shows rapid replication in human primary nasal epithelial cultures and efficiently uses the endosomal route of entry. BioRxiv **10**(2021.12), 31–474653 (2022)

Peng, X., Zhou, Y., Nie, K., Zhou, F., Yuan, Y., Song, J., Qu, J.: Promising near-infrared plasmonic biosensor employed for specific detection of SARS-CoV-2 and its spike glycoprotein. New J. Phys. **22**(10), 103046 (2020)

Phan, T., Boes, S., McCullough, M., Gribschaw, J., Marsh, J., Harrison, L.H., Wells, A.: Development of a one-step qualitative RT-PCR assay to detect the SARS-CoV-2 Omicron (B. 1.1. 529) variant in respiratory specimens. J. Clin. Microbiol. **60**(3), e00024-22 (2022)

Qureshi, A.I., Saeed, O., Syed, U. (eds.): Coronavirus disease: from origin to outbreak. Academic Press, New York (2021)

Rahman, M.S., Anower, M.S., Hasan, M.R., Hossain, M.B., Haque, M.I.: Design and numerical analysis of highly sensitive Au-MoS2-graphene based hybrid surface plasmon resonance biosensor. Opt. Commun. **396**, 36–43 (2017)

Rahman, M.S., Anower, M.S., Hasan, M.R., Hossain, M.B., Haque, M.I.: Design and numerical analysis of highly sensitive Au-MoS2-graphene based hybrid surface plasmon resonance biosensor. Optics Commun. **396**, 36–43 (2017)

Rahman, M.M., Rana, M.M., Rahman, M.S., Anower, M.S., Mollah, M.A., Paul, A.K.: Sensitivity enhancement of SPR biosensors employing heterostructure of PtSe2 and 2D materials. Opt. Mater. **107**, 110123 (2020)

Rahman, M.M., Abdulrazak, L.F., Ahsan, M., Based, M.A., Rana, M.M., Anower, M.S., Rikta, K.A., Haider, J., Gurusamy, S.: 2D nanomaterial-based hybrid structured (Au-WSe 2-PtSe 2-BP) surface plasmon resonance (SPR) sensor with improved performance. IEEE Access **10**, 689–698 (2021)

Rikta, K.A., Anower, M.S., Rahman, M.S., Rahman, M.M.: SPR biosensor using SnSe-phosphorene heterostructure. Sens. Bio-Sens. Res. **33**, 100442 (2021)

Saad, M.: Fluoride glass fiber: state of the art. Fiber Optic Sens. Appl. VI **7316**, 170–185 (2009)

Singh, S., Prajapati, Y.K.: TiO2/gold-graphene hybrid solid core SPR based PCF RI sensor for sensitivity enhancement. Optik **224**, 165525 (2020)

Song, B., Li, D., Qi, W., Elstner, M., Fan, C., Fang, H.: Graphene on Au (111): a highly conductive material with excellent adsorption properties for high-resolution bio/nanodetection and identification. ChemPhysChem **11**(3), 585–589 (2010)

Talebian, S., Wallace, G.G., Schroeder, A., Stellacci, F., Conde, J.: Nanotechnology-based disinfectants and sensors for SARS-CoV-2. Nat. Nanotechnol. **15**(8), 618–621 (2020)

Thakallapelli, A., Ghosh, S., Kamalasadan, S.: Real-time frequency based reduced order modeling of large power grid. In: 2016 IEEE Power and Energy Society General Meeting (PESGM) (pp. 1–5). IEEE (2016)

Tumolo, T., Angnes, L., Baptista, M.S.: Determination of the refractive index increment (dn/dc) of molecule and macromolecule solutions by surface plasmon resonance. Anal. Biochem. **333**(2), 273–279 (2004)

Uniyal, A., Chauhan, B., Pal, A., Srivastava, V.: InP and graphene employed surface plasmon resonance sensor for measurement of sucrose concentration: a numerical approach. Opt. Eng. **61**(5), 057103–057103 (2022a)

Uniyal, A., Chauhan, B., Pal, A., Singh, Y.: Surface plasmon biosensor based on Bi 2 Te 3 antimonene heterostructure for the detection of cancer cells. Appl. Opt. **61**(13), 3711–3719 (2022b)

Wang, M., Huo, Y., Jiang, S., Zhang, C., Yang, C., Ning, T., Liu, X., Li, C., Zhang, W., Man, B.: Theoretical design of a surface plasmon resonance sensor with high sensitivity and high resolution based on graphene–WS 2 hybrid nanostructures and Au–Ag bimetallic film. RSC Adv. **7**(75), 47177–47182 (2017)

Wang, T., Zhang, M., Liu, K., Jiang, J., Zhao, Y., Ma, J., Liu, T.: The effect of the TiO2 film on the performance of the optical fiber SPR sensor. Optics Communications **448**, 93–97 (2019)

Wang, M., Fu, A., Hu, B., Tong, Y., Liu, R., Liu, Z., Gu, J., Xiang, B., Liu, J., Jiang, W., Shen, G.: Nanopore targeted sequencing for the accurate and comprehensive detection of SARS-CoV-2 and other respiratory viruses. Small **16**(32), 2002169 (2020)

Wee, S.K., Sivalingam, S.P., Yap, E.P.H.: Rapid direct nucleic acid amplification test without RNA extraction for SARS-CoV-2 using a portable PCR thermocycler. Genes **11**(6), 664 (2020)

Weir, R.A.: Letter by Weir Regarding Article, "Angiotensin-converting enzyme 2: SARS-CoV-2 receptor and regulator of the renin-angiotensin system: celebrating the 20th anniversary of the discovery of ACE2." Circ. Res. **127**(2), e44–e45 (2020)

Wong, S.K., Li, W., Moore, M.J., Choe, H., Farzan, M.: A 193-amino acid fragment of the SARS coronavirus S protein efficiently binds angiotensin-converting enzyme 2. J. Biol. Chem. **279**(5), 3197–3201 (2004)

World Health Organization (WHO): Novel Coronavirus 2019 (COVID-19). World Health Organization, Geneva, Switzerland (2022)

Wu, L., Chu, H.S., Koh, W.S., Li, E.P.: Highly sensitive graphene biosensors based on surface plasmon resonance. Opt. Express **18**(14), 14395–14400 (2010)

Wu, L., Guo, J., Wang, Q., Lu, S., Dai, X., Xiang, Y., Fan, D.: Sensitivity enhancement by using few-layer black phosphorus-graphene/TMDCs heterostructure in surface plasmon resonance biochemical sensor. Sens. Actuators B Chem. **249**, 542–548 (2017)

Xu, Y., Li, X., Zhu, B., Liang, H., Fang, C., Zhang, H., Liu, H., Xia, H., Tang, J., Zhang, K., Gong, S.: Characteristics of pediatric SARS-CoV-2 infection and potential evidence for persistent fecal viral shedding. Nat Med **26**, 502–505 (2020)

Yadav, S., Jain, P.: Real time cost effective e-saline monitoring and control system. In: 2016 International Conference on Control, Computing, Communication and Materials (ICCCM) (pp. 1–4). IEEE (2016)

Yesudasu, V., Pradhan, H.S.: Performance enhancement of a novel surface plasmon resonance biosensor using thallium bromide. IEEE Trans. Nanobiosci. **21**(2), 206–215 (2021)

Yolshin N, Varchenko K, Komissarova K, Danilenko D, Komissarov A, Lioznov D (2021) One-step RT-PCR Ins214EPE assay for Omicron (B.1.1.529) variant detection. https://www.protocols.io/view/one-step-rt-pcr-ins214epe-assay-for-omicron-b-1-1-b2trqem6.

Zeng, S., Hu, S., Xia, J., Anderson, T., Dinh, X.Q., Meng, X.M., Coquet, P., Yong, K.T.: Graphene–MoS2 hybrid nanostructures enhanced surface plasmon resonance biosensors. Sens. Actuators B Chem. **207**, 801–810 (2015)

Zhang, Z., Zhao, P., Sun, F., Xiao, G., Wu, Y.: Self-referencing in optical-fiber surface plasmon resonance sensors. IEEE Photonics Technol. Lett. **19**(24), 1958–1960 (2007)

Zhang, J., Mai, X., Hong, X., Chen, Y., Li, X.: Optical fiber SPR biosensor with a solid-phase enzymatic reaction device for glucose detection. Sens. Actuators B Chem. **366**, 131984 (2022)

Zhu, W., Kong, L., Long, W., Shi, X., Zhou, D., Sun, L., Zhou, L., Yang, G., Liu, X., Liu, H., Bo, M.: Band Structure engineering of black phosphorus/graphene/MoS2 van der Waals heterojunctions for photovoltaic and optoelectronic device application. J. Phys. Conf. Ser. **1865**(2), 022021 (2021)

Authors and Affiliations

**Tarik Bin Abdul Akib[1,2] · Shahriar Mostufa[1] · Md. Masud Rana[1] ·
Md. Biplob Hossain[3,4] · Md. Rabiul Islam[3]**

Tarik Bin Abdul Akib
abdulakibruhe@gmail.com

Shahriar Mostufa
shahriarmostufa@gmail.com

Md. Masud Rana
md.masud.rana.ruet@gmail.com

Md. Rabiul Islam
mrislam@uow.edu.au

[1]　Department of Electrical and Electronic Engineering, Rajshahi University of Engineering
and Technology, Rajshahi 6204, Bangladesh

[2]　Department of Electrical and Electronic Engineering, Bangladesh Army University of Engineering
and Technology, Rajshahi 6431, Bangladesh

[3]　Faculty of Engineering and Information Sciences, University of Wollongong, Wollongong,
NSW 2522, Australia

[4]　Department of Electrical and Electronic Engineering, Jashore University of Science
and Technology, Jashore 7408, Bangladesh